

# Correlated-Electron Systems and High-Temperature Superconductivity

Takashi Yanagisawa<sup>a</sup>, Mitake Miyazaki<sup>b</sup> and Kunihiko Yamaji<sup>a</sup>

<sup>a</sup>*Electronics and Photonics Research Group, National Institute of Advanced Industrial Science and Technology (AIST), Tsukuba Central 2, 1-1-1 Umezono, Tsukuba, Ibaraki 305-8568, Japan*

<sup>b</sup>*Hakodate National College of Technology, 14-1 Tokura, Hakodate 042-8501, Japan*

## ABSTRACT

We present recent theoretical results on superconductivity in correlated-electron systems, especially in the two-dimensional Hubbard model and the three-band d-p model. The mechanism of superconductivity in high-temperature superconductors has been extensively studied on the basis of various electronic models and also electron-phonon models. In this study we investigate the properties of superconductivity in correlated-electron systems by using numerical methods such as the variational Monte Carlo method and the quantum Monte Carlo method.

The Hubbard model is one of basic models for strongly correlated electron systems, and is regarded as the model of cuprate high temperature superconductors. The d-p model is more realistic model for cuprates. The superconducting condensation energy obtained by adopting the Gutzwiller ansatz is in reasonable agreement with the condensation energy estimated for  $\text{YBa}_2\text{Cu}_3\text{O}_7$ . We show the phase diagram of the ground state using this method. We have further investigated the stability of striped and checkerboard states in the under-doped region. Holes doped in a half-filled square lattice lead to an incommensurate spin and charge density wave. The relationship of the hole density  $x$  and incommensurability  $\delta$ ,  $\delta \sim x$ , is satisfied in the lower doping region, as indicated by the variational Monte Carlo calculations for the two-dimensional Hubbard model. A checkerboard-like charge-density modulation with a roughly  $4 \times 4$  period has also been observed by scanning tunneling microscopy experiments in Bi2212 and Na-CCOC compounds. We have performed a variational Monte Carlo simulation on a two-dimensional  $t$ - $t'$ - $t''$ - $U$  Hubbard model with a Bi-2212 type band structure and found that the  $4 \times 4$  period checkerboard spin modulation, that is characterized by multi Q vectors, is indeed stabilized.

We have further performed an investigation by using a quantum Monte Carlo method which is a numerical method that can be used to simulate the behavior of correlated electron systems. We present a new algorithm of the quantum Monte Carlo diagonalization that is a method for the evaluation of expectation value without the negative sign problem. We compute pair correlation functions and show that pair correlation is indeed enhanced with hole doping.

Key words: High-temperature superconductivity, strongly correlated electrons, Monte Carlo methods, Hubbard model, condensation energy, pair-correlation function

## I. INTRODUCTION

The effect of the strong correlation between electrons is important for many quantum critical phenomena, such as unconventional superconductivity (SC) and the metal-insulator transition. Typical correlated electron systems are high-temperature superconductors[1–5], heavy fermions[6–9] and organic conductors[10]. The phase diagram for the typical high- $T_c$  cuprates is shown in Fig.1.[9] It has a characteristics that the region of antiferromagnetic order exists at low carrier concentrations and the superconducting phase is adjacent to the antiferromagnetism.

In the low-carrier region shown in Fig.2 there is the anomalous metallic region where the susceptibility and  $1/T_1$  show a peak above  $T_c$  suggesting an existence of the pseudogap. To clarify an origin of the anomalous metallic behaviors is also a subject attracting many physicists as a challenging problem.

It has been established that the Cooper pairs of high- $T_c$  cuprates have the  $d$ -wave symmetry in the hole-doped materials.[11, 12] Several evidences of  $d$ -wave pairing symmetry were provided for the electron-doped cuprates  $\text{Nd}_{2-x}\text{Ce}_x\text{CuO}_4$ . [13–15] Thus it is expected that the superconductivity of electronic origin is a candidate for the high- $T_c$  superconductivity. We can also expect that the origin of  $d$ -wave superconductivity lies in the on-site Coulomb interaction of the two-dimensional Hubbard model.

The antiferromagnetism should also be examined in correlated electron systems. The undoped oxide compounds exhibit rich structures of antiferromagnetic correlations over a wide range of temperature that are described by the two-dimensional quantum antiferromagnetism.[16–18] A small number of holes introduced by doping are responsible for the disappearance of long-range antiferromagnetic order.[19–24]

Recent neutron scattering experiments have suggested an existence of incommensurate ground states with mod-

ulation vectors given by  $Q_s = (\pi \pm 2\pi\delta, \pi)$  and  $Q_c = (\pm 4\pi\delta, 0)$  (or  $Q_s = (\pi, \pi \pm 2\pi\delta)$  and  $Q_c = (0, \pm 4\pi\delta)$ ) where  $\delta$  denotes the hole-doping ratio.[25] We can expect that the incommensurate correlations are induced by holes doped into the Cu-O plane in the underdoped region. A checkerboard-like charge-density modulation with a roughly  $4 \times 4$  period has also been observed by scanning tunneling microscopy experiments in Bi2212 and Na-CCOC compounds.

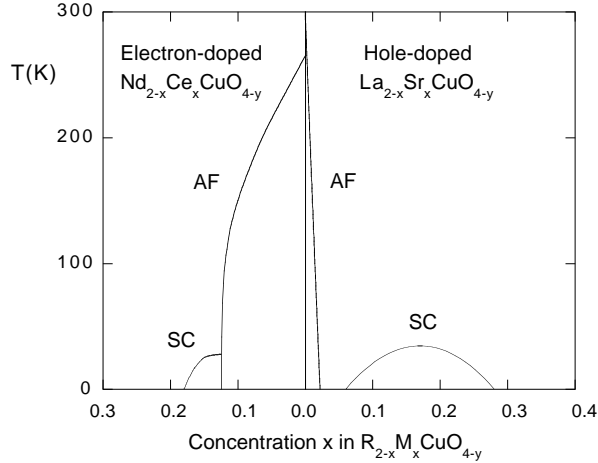


FIG. 1: Phase diagram delineating the regions of superconductivity and antiferromagnetic ordering of the  $Cu^{2+}$  ions for the hole-doped  $La_{2-x}Sr_xCuO_4$  and electron-doped  $Nd_{2-x}Ce_xCuO_{4-y}$  systems.

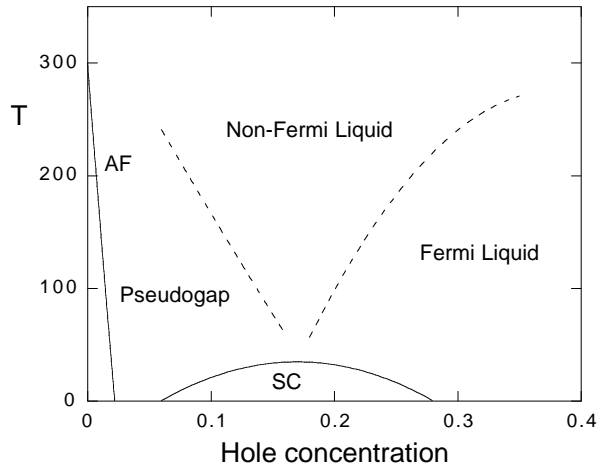


FIG. 2: Phase diagram showing the regions of non-Fermi liquid and pseudogap metal for the hole-doped case. The boundaries indicated in the figure are not confirmed yet.

Recently the mechanism of superconductivity in high-temperature superconductors has been extensively studied using various two-dimensional (2D) models of electronic interactions. Among them the 2D Hubbard model[26] is the simplest and most fundamental model. This model has been studied intensively using numer-

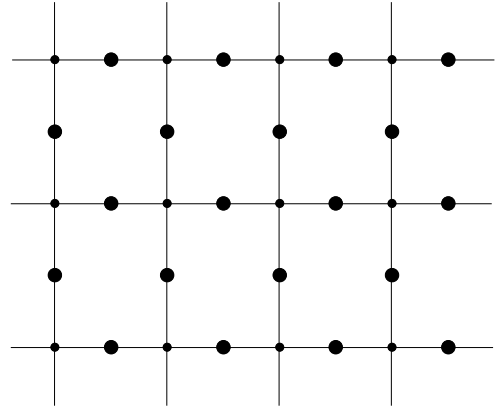


FIG. 3: The lattice of the three-band Hubbard model on the  $CuO_2$  plane. Small circles denote Cu sites and large ones denote O sites.

ical tools, such as the Quantum Monte Carlo method [27–42], and the variational Monte Carlo method[24, 43–50]. The two-leg ladder Hubbard model was also investigated with respect to the mechanism of high-temperature superconductivity[51–59].

Since the discovery of cuprate high-temperature superconductors, many researchers have tried to explain the occurrence of superconductivity of these materials in terms of the two-dimensional (2D) Hubbard model. However, it remains matter of considerable controversial as to whether the 2D Hubbard model accounts for the properties of high-temperature cuprate superconductors. This is because the membership of the the two-dimensional Hubbard model in the category of strongly correlated systems is a considerable barrier to progress on this problem. The quest for the existence of a superconducting transition in the 2D Hubbard model is a long-standing problem in correlated-electron physics, and has been the subject of intensive study[35, 36, 38, 46, 60, 61]. In particular, the results of quantum Monte Carlo methods, which are believed to be exact unbiased methods, have failed to show the existence of superconductivity in this model[38, 61].

In the weak coupling limit we can answer this question. We can obtain the superconducting order parameter of the Hubbard model in the limit of small  $U$ , that is given by[62–66]

$$\Delta = \exp\left(-\frac{2}{xU^2}\right), \quad (1)$$

where  $U$  is the strength of the on-site Coulomb interaction and the exponent  $x$  is determined by solving the gap equation. Thus the existence of the superconducting gap is guaranteed by the weak coupling theory although  $\Delta$  is extremely small because of the exponential behavior

given above.  $x$  indicates the strength of superconductivity. In the intermediate or large coupling region, we must study it beyond the perturbation theory.

We investigate the ground state of the Hubbard model by employing the variational Monte Carlo method. In the region  $6 \leq U \leq 12$ , the finite superconducting gap is obtained by using the quantum variational Monte Carlo method. The superconducting condensation energy obtained by adopting the Gutzwiller ansatz is in reasonable agreement with the condensation energy derived for  $\text{YBa}_2\text{Cu}_3\text{O}_7$ . We have further investigated the stability of striped and checkerboard states in the under-doped region. Holes doped in a half-filled square lattice lead to an incommensurate spin and charge density wave. The relationship of the hole density  $x$  and incommensurability  $\delta$ ,  $\delta \sim x$ , is satisfied in the lower doping region. This is consistent with the results by neutron scattering measurements. To examine the stability of a  $4 \times 4$  checkerboard state, we have performed a variational Monte Carlo simulation on a two-dimensional  $t-t'-t''-U$  Hubbard model with a Bi-2212 type band structure. We found that the  $4 \times 4$  period checkerboard checkerboard spin modulation that is characterized by multi  $Q$  vectors is stabilized.

Further investigation has been performed by using the quantum Monte Carlo method which is a numerical method that can be used to simulate the behavior of correlated electron systems. This method is believed to be an exact unbiased method. We compute pair correlation functions to examine a possibility of superconductivity.

The Quantum Monte Carlo (QMC) method is a numerical method employed to simulate the behavior of correlated electron systems. It is well known, however, that there are significant issues associated with the application to the QMC. First, the standard Metropolis(or heat bath) algorithm is associated with the negative sign problem. Second, the convergence of the trial wave function is sometimes not monotonic, and further, is sometimes slow. In past studies, workers have investigated the possibility of eliminating the negative sign problem[37, 38, 40–42]. We present the results obtained by a method, quantum Monte Carlo diagonalization, without the negative sign problem.

## II. HUBBARD HAMILTONIAN

The Hubbard Hamiltonian is

$$H = - \sum_{ij} t_{ij} c_{i\sigma}^\dagger c_{i\sigma} + U \sum_i n_{i\uparrow} n_{i\downarrow}, \quad (2)$$

where  $c_{i\sigma}^\dagger$  and  $c_{i\sigma}$  denote the creation and annihilation operators of electrons, respectively, and  $n_{i\sigma} = c_{i\sigma}^\dagger c_{i\sigma}$  is the number operator. The second term represents the on-site Coulomb interaction which acts when the two electrons occupy the same site. The numbers of lattice sites and electrons are denoted as  $N$  and  $N_e$ , respectively. The electron density is  $n_e = N_e/N$ .

In the non-interacting limit  $U = 0$ , the Hamiltonian is easily diagonalized in terms of the Fourier transformation. In the ground state each energy level is occupied by electrons up to the Fermi energy. In the other limit  $t_{ij} = 0$ , each site is occupied by the up- or down-spin electron, or is empty. The non-zero  $t_{ij}$  induces the movement of electrons that leads to a metallic state if  $N_e \neq N$ . The ground state is probably insulating at half-filling  $N_e = N$  if  $U$  is sufficiently large.

If  $t_{ij} = t$  are non-zero only for the nearest-neighbor pairs, the Hubbard Hamiltonian is transformed to the following effective Hamiltonian for large  $U/t$ : [67]

$$\begin{aligned} H = & -t \sum_{\langle ij \rangle \sigma} a_{i\sigma}^\dagger a_{j\sigma} - \frac{t^2}{U} \sum_{\mu\mu'} [a_{j+\mu\uparrow}^\dagger a_{j\downarrow}^\dagger a_{j\downarrow} a_{j+\mu'\uparrow} \\ & + a_{j\uparrow}^\dagger a_{j+\mu\downarrow}^\dagger a_{j+\mu'\downarrow} a_{j\uparrow} + a_{j+\mu\uparrow}^\dagger a_{j\downarrow}^\dagger a_{j+\mu'\downarrow} a_{j\uparrow} \\ & + a_{j\uparrow}^\dagger a_{j+\mu\downarrow}^\dagger a_{j\downarrow} a_{j+\mu'\uparrow}], \end{aligned} \quad (3)$$

where  $a_{i\sigma} = c_{i\sigma}(1 - n_{i,-\sigma})$  and  $j + \mu$  and  $j + \mu'$  indicate the nearest-neighbor sites in the  $\mu$  and  $\mu'$  directions, respectively. The second term contains the three-site terms when  $\mu \neq \mu'$ . If we neglect the three-site terms, this effective Hamiltonian is reduced to the t-J model:

$$H = -t \sum_{\langle ij \rangle \sigma} (a_{i\sigma}^\dagger a_{j\sigma} + \text{h.c.}) + J \sum_{\langle ij \rangle} (\mathbf{S}_i \cdot \mathbf{S}_j - \frac{1}{4} n_i n_j),$$

where  $J = 4t^2/U$ .

The Hubbard model has a long history in describing the magnetism of materials since the early works by Hubbard[26], Gutzwiller[68] and Kanamori.[69] One-dimensional Hubbard model has been well understood by means of the Bethe ansatz[70–72] and conformal field theory.[73–75] The solutions established a novel concept of the Tomonaga-Luttinger liquid[76] which is described by the scalar bosons corresponding to charge and spin sectors, respectively. The correlated electrons in two- and three-dimensional space are still far from a complete understanding in spite of the success for the one-dimensional Hubbard model. A possibility of superconductivity is a hot topic as well as the magnetism and metal-insulator transition for the two- and three-dimensional Hubbard model.

The three-band Hubbard model that contains  $d$  and  $p$  orbitals has also been investigated intensively with respect to high temperature superconductors. [24, 64, 77–88] This model is also called the d-p model. The 2D three-band Hubbard model is the more realistic and relevant model for two-dimensional  $\text{CuO}_2$  planes which are contained usually in the crystal structures of high- $T_c$  superconductors. The network of  $\text{CuO}_2$  layer is shown in Fig.3. The parameters of the three-band Hubbard model are given by the Coulomb repulsion  $U_d$ , energy levels of  $p$  electrons  $\epsilon_p$  and  $d$  electron  $\epsilon_d$ , and transfer between  $p$  orbitals given by  $t_{pp}$ . Typical parameter values for the three-band ( $d$ - $p$ ) Hubbard model are shown in Table I.

The Hamiltonian of the three-band Hubbard model is written as[24, 47, 48, 80]

$$\begin{aligned}
H_{dp} = & \epsilon_d \sum_{i\sigma} d_{i\sigma}^\dagger d_{i\sigma} + U_d \sum_i d_{i\uparrow}^\dagger d_{i\uparrow} d_{i\downarrow}^\dagger d_{i\downarrow} \\
& + \epsilon_p \sum_{i\sigma} (p_{i+\hat{x}/2,\sigma}^\dagger p_{i+\hat{x}/2,\sigma} + p_{i+\hat{y}/2,\sigma}^\dagger p_{i+\hat{y}/2,\sigma}) \\
& - t_{dp} \sum_{i\sigma} [d_{i\sigma}^\dagger (p_{i+\hat{x}/2,\sigma} + p_{i+\hat{y}/2,\sigma} - p_{i-\hat{x}/2,\sigma} \\
& - p_{i-\hat{y}/2,\sigma}) + \text{h.c.}] \\
& - t_{pp} \sum_{i\sigma} [p_{i+\hat{y}/2,\sigma}^\dagger p_{i+\hat{x}/2,\sigma} - p_{i+\hat{y}/2,\sigma}^\dagger p_{i-\hat{x}/2,\sigma} \\
& - p_{i-\hat{y}/2,\sigma}^\dagger p_{i+\hat{x}/2,\sigma} + p_{i-\hat{y}/2,\sigma}^\dagger p_{i-\hat{x}/2,\sigma} \\
& + \text{h.c.}]. \tag{4}
\end{aligned}$$

$\hat{x}$  and  $\hat{y}$  represent unit vectors along x and y directions, respectively.  $p_{i\pm\hat{x}/2,\sigma}^\dagger$  and  $p_{i\pm\hat{x}/2,\sigma}$  denote the operators for the  $p$  electrons at site  $R_i \pm \hat{x}/2$ . Similarly  $p_{i\pm\hat{y}/2,\sigma}^\dagger$  and  $p_{i\pm\hat{y}/2,\sigma}$  are defined.  $U_d$  denotes the strength of Coulomb interaction between  $d$  electrons. For simplicity we neglect the Coulomb interaction among  $p$  electrons in this paper. Other notations are standard and energies are measured in  $t_{dp}$  units. The number of cells is denoted as  $N$  for the three-band Hubbard model. In the non-interacting case ( $U_d = 0$ ) the Hamiltonian in the  $\mathbf{k}$ -space is written as:

$$\begin{aligned}
H_{dp}^0 = & \epsilon_d \sum_{\mathbf{k}\sigma} d_{\mathbf{k}\sigma}^\dagger d_{\mathbf{k}\sigma} + \epsilon_p \sum_{\mathbf{k}\sigma} (p_{x\mathbf{k}\sigma}^\dagger p_{x\mathbf{k}\sigma} + p_{y\mathbf{k}\sigma}^\dagger p_{y\mathbf{k}\sigma}) \\
& + \sum_{\mathbf{k}\sigma} (2it_{dp} \sin(k_x/2) d_{\mathbf{k}\sigma}^\dagger p_{x\mathbf{k}\sigma} + \text{h.c.}) \\
& + \sum_{\mathbf{k}\sigma} (2it_{dp} \sin(k_y/2) d_{\mathbf{k}\sigma}^\dagger p_{y\mathbf{k}\sigma} + \text{h.c.}) \\
& + \sum_{\mathbf{k}\sigma} (-4t_{pp} \sin(k_x/2) \sin(k_y/2)) (p_{x\mathbf{k}\sigma}^\dagger p_{y\mathbf{k}\sigma} + \text{h.c.}), \tag{5}
\end{aligned}$$

where  $d_{\mathbf{k}\sigma}$  ( $d_{\mathbf{k}\sigma}^\dagger$ ),  $p_{x\mathbf{k}\sigma}$  ( $p_{x\mathbf{k}\sigma}^\dagger$ ) and  $p_{y\mathbf{k}\sigma}$  ( $p_{y\mathbf{k}\sigma}^\dagger$ ) are operators for  $d$ -,  $p_x$ - and  $p_y$ -electron of the momentum  $\mathbf{k}$  and spin  $\sigma$ , respectively.

In the limit  $t_{dp} \ll U_d - (\epsilon_p - \epsilon_d)$ ,  $t_{dp} \ll \epsilon_p - \epsilon_d$ , and  $\epsilon_p - \epsilon_d < U_d$ , the  $d$ - $p$  model is mapped to the t-J model with

$$J = 4t_{eff}^2 \left( \frac{1}{U_d} + \frac{2}{2(\epsilon_p - \epsilon_d) + U_p} \right), \tag{6}$$

where  $t_{eff} \simeq t_{dp}^2 / (\epsilon_p - \epsilon_d)$ .  $J_K = 4t_{eff}$  gives the anti-ferromagnetic coupling between the neighboring  $d$  and  $p$  electrons. In real materials  $(\epsilon_p - \epsilon_d) / t_{dp}$  is not so large. Thus it seems that the mapping to the t-J model is not necessarily justified.

### III. VARIATIONAL MONTE CARLO STUDIES

In this Section we present studies on the two-dimensional Hubbard model by using the variational

TABLE I: Typical parameter values for the three-band Hubbard model. Energies are measured in eV.

	Ref.[89]	Ref.[90]	Ref.[91]	Ref.[78]
$\epsilon_p - \epsilon_d$	3.6	2.75 - 3.75	3.5	2.5
$t_{dp}$	1.3	1.5	1.5	1.47
$t_{pp}$	0.65	0.65	0.6	
$U_d$	10.5	8.8	9.4	9.7
$U_p$	4.0	6.0	4.7	5.7
$U_{dp}$	1.2	<1.0	0.8	<1

Monte Carlo method.

#### A. Variational Monte Carlo Method

Let us start by describing the method based on the 2D Hubbard model. The Hamiltonian is given by

$$\begin{aligned}
H = & -t \sum_{\langle ij \rangle \sigma} (c_{i\sigma}^\dagger c_{j\sigma} + \text{h.c.}) - t' \sum_{\langle\langle j\ell \rangle\rangle \sigma} (c_{j\sigma}^\dagger c_{\ell\sigma} + \text{h.c.}) \\
& + U \sum_j n_{j\uparrow} n_{j\downarrow}, \tag{7}
\end{aligned}$$

where  $\langle ij \rangle$  denotes summation over all the nearest-neighbor bonds and  $\langle\langle j\ell \rangle\rangle$  means summation over the next nearest-neighbor pairs.  $t$  is our energy unit. The dispersion is given by

$$\epsilon_{\mathbf{k}} = -2t(\cos(k_x) + \cos(k_y)) - 4t' \cos(k_x) \cos(k_y). \tag{8}$$

Our trial wave function is the Gutzwiller-projected wave functions defined as

$$\psi_n = P_{N_e} P_G \psi_0, \tag{9}$$

$$\psi_s = P_{N_e} P_G \psi_{BCS}, \tag{10}$$

where

$$\psi_0 = \prod_{|\mathbf{k}| \leq k_F, \sigma} c_{\mathbf{k}\sigma}^\dagger |0\rangle, \tag{11}$$

$$\psi_{BCS} = \prod_{\mathbf{k}} (u_{\mathbf{k}} + v_{\mathbf{k}} c_{\mathbf{k}\uparrow}^\dagger c_{-\mathbf{k}\downarrow}^\dagger) |0\rangle. \tag{12}$$

$P_G$  is the Gutzwiller projection operator given by

$$P_G = \prod_j [1 - (1-g)n_{j\uparrow} n_{j\downarrow}]; \tag{13}$$

$g$  is a variational parameter in the range from 0 to unity and  $j$  labels a site in the real space.  $P_{N_e}$  is a projection operator which extracts only the sites with a fixed total electron number  $N_e$ . Coefficients  $u_{\mathbf{k}}$  and  $v_{\mathbf{k}}$  in  $\psi_{BCS}$  appear in the ratio defined by

$$\frac{v_{\mathbf{k}}}{u_{\mathbf{k}}} = \frac{\Delta_{\mathbf{k}}}{\xi_{\mathbf{k}} + (\xi_{\mathbf{k}}^2 + \Delta_{\mathbf{k}}^2)^{1/2}}, \tag{14}$$

where  $\xi_{\mathbf{k}} = \epsilon_{\mathbf{k}} - \mu$  and  $\Delta_{\mathbf{k}}$  is a  $\mathbf{k}$ -dependent gap function.  $\mu$  is a variational parameter working like the chemical

potential.  $c_{\mathbf{k}\sigma}$  is the Fourier transform of  $c_{j\sigma}$ . The wave functions  $\psi_n$  and  $\psi_s$  are expressed by the Slater determinants for which the expectations values are evaluated using a Monte Carlo procedure.[43, 44, 92]  $\psi_s$  is written as

$$\begin{aligned}\psi_s &\propto P_{N_e} P_G \exp\left[\sum_{\mathbf{k}} (v_{\mathbf{k}}/u_{\mathbf{k}}) c_{\mathbf{k}\uparrow}^\dagger c_{-\mathbf{k}\downarrow}^\dagger\right] |0\rangle \\ &= P_{N_e} P_G \exp\left[\sum_{j\ell} a(j, \ell) c_{j\uparrow}^\dagger c_{\ell\downarrow}^\dagger\right] |0\rangle \\ &\propto P_G \left[\sum_{j\ell} a(j, \ell) c_{j\uparrow}^\dagger c_{\ell\downarrow}^\dagger\right]^{N_e/2} |0\rangle,\end{aligned}\quad (15)$$

where

$$a(j, \ell) = (1/N) \sum_{\mathbf{k}} (v_{\mathbf{k}}/u_{\mathbf{k}}) \exp[i\mathbf{k} \cdot (\mathbf{R}_\ell - \mathbf{R}_j)]. \quad (16)$$

Then  $\psi_s$  is written using the Slater determinants as

$$\begin{aligned}\psi_s &= P_G \sum_{j_1 \cdots j_{N_e/2} \ell_1 \cdots \ell_{N_e/2}} \\ &A(j_1 \cdots j_{N_e/2}, \ell_1 \cdots \ell_{N_e/2}) \\ &\times c_{j_1\uparrow}^\dagger c_{j_2\uparrow}^\dagger \cdots c_{j_{N_e/2}\uparrow}^\dagger c_{\ell_1\downarrow}^\dagger c_{\ell_2\downarrow}^\dagger \cdots c_{\ell_{N_e/2}\downarrow}^\dagger |0\rangle,\end{aligned}\quad (17)$$

where  $A(j_1 \cdots j_{N_e/2}, \ell_1 \cdots \ell_{N_e/2})$  is the Slater determinant defined by

$$A(j_1 \cdots \ell_{N_e/2}) = \begin{vmatrix} a(j_1, \ell_1) & a(j_1, \ell_2) & \cdots & a(j_1, \ell_{N_e/2}) \\ a(j_2, \ell_1) & a(j_2, \ell_2) & \cdots & a(j_2, \ell_{N_e/2}) \\ \cdots & \cdots & \cdots & \cdots \\ a(j_{N_e/2}, \ell_1) & a(j_{N_e/2}, \ell_2) & \cdots & a(j_{N_e/2}, \ell_{N_e/2}) \end{vmatrix}. \quad (18)$$

In the process of Monte Carlo procedure the values of cofactors of the matrix in eq.(18) are stored and corrected at each time when the electron distribution is modified. We optimized the ground state energy

$$E_g = \langle H \rangle = \langle \psi_s | H | \psi_s \rangle / \langle \psi_s | \psi_s \rangle \quad (19)$$

with respect to  $g$ ,  $\Delta_{\mathbf{k}}$  and  $\mu$  for  $\psi_s$  for  $\psi_s$ . For  $\psi_n$  the variational parameter is only  $g$ . We can employ the correlated measurements method[93] in the process of searching optimal parameter values minimizing  $E_g$ .

A Monte Carlo algorithm developed in the auxiliary field quantum Monte Carlo calculations can also be employed in evaluating the expectation values for the wave functions shown above.[94–96] Note that the Gutzwiller projection operator is written as

$$P_G = \exp(-\alpha \sum_i n_{i\uparrow} n_{i\downarrow}), \quad (20)$$

where  $\alpha = \log(1/g)$ . Then using the discrete Hubbard-Stratonovich transformation, the Gutzwiller operator is

the bilinear form:

$$\begin{aligned}\exp(-\alpha \sum_i n_{i\uparrow} n_{i\downarrow}) &= (1/2)^N \sum_{\{s_i\}} \exp[2a \\ &\times \sum_i s_i (n_{i\uparrow} - n_{i\downarrow}) - \frac{\alpha}{2} \sum_i (n_{i\uparrow} + n_{i\downarrow})],\end{aligned}\quad (21)$$

where  $\cosh(2a) = e^{\alpha/2}$ . The Hubbard-Stratonovich auxiliary field  $s_i$  takes the values of  $\pm 1$ . The norm  $\langle \psi_n | \psi_n \rangle$  is written as

$$\begin{aligned}\langle \psi_n | \psi_n \rangle &= \text{const.} \sum_{\{u_i\} \{s_i\}} \prod_{\sigma} \det(\phi_0^{\sigma\dagger} \exp(V^\sigma(u, \alpha)) \\ &\times \exp(V^\sigma(s, \alpha)) \phi_0^\sigma),\end{aligned}\quad (22)$$

where  $V^\sigma(s, \alpha)$  is a diagonal  $N \times N$  matrix corresponding to the potential

$$h^\sigma(s) = 2a\sigma \sum_i s_i n_{i\sigma} - \frac{\alpha}{2} \sum_i n_{i\sigma}. \quad (23)$$

$V^\sigma(s, \alpha)$  is written as

$$V^\sigma(s, \alpha) = \text{diag}(2a\sigma s_1 - \alpha/2, \cdots, 2a\sigma s_N - \alpha/2, 0, \cdots), \quad (24)$$

where  $\text{diag}(a, \cdots)$  denotes a diagonal matrix with elements given by the arguments  $a, \cdots$ . The elements of  $(\phi_0^\sigma)_{ij}$  ( $i = 1, \cdots, N; j = 1, \cdots, N_e/2$ ) are given by linear combinations of plane waves. For example,

$$(\phi_0^\sigma)_{ij} = \exp(i\mathbf{r}_i \cdot \mathbf{k}_j). \quad (25)$$

Then we can apply the standard Monte Carlo sampling method to evaluate the expectation values.[94, 95] This method is used to consider an off-diagonal Jastrow correlation factor of  $\exp(-S)$ -type. The results for the improved wave functions are discussed in Section III.J.

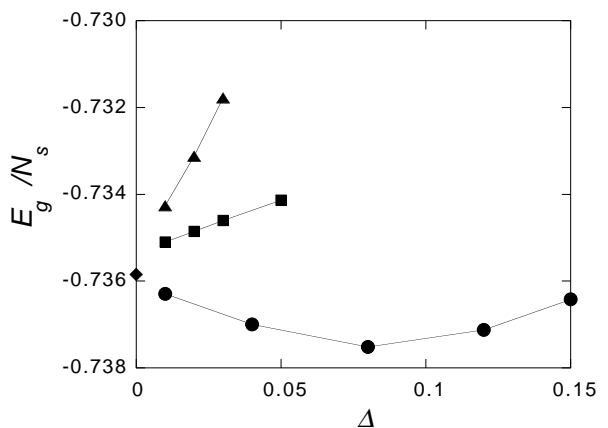


FIG. 4: Ground state energy per site  $E_g/N$  for the 2D Hubbard model is plotted against  $\Delta$  for the case of 84 electrons on the  $10 \times 10$  lattice with  $U = 8$  and  $t' = 0$ . Solid curves are for the  $d$ -wave gap function. Squares and triangles are for the  $s^*$ - and  $s$ -wave gap functions, respectively. The diamond shows the normal state value.[46]

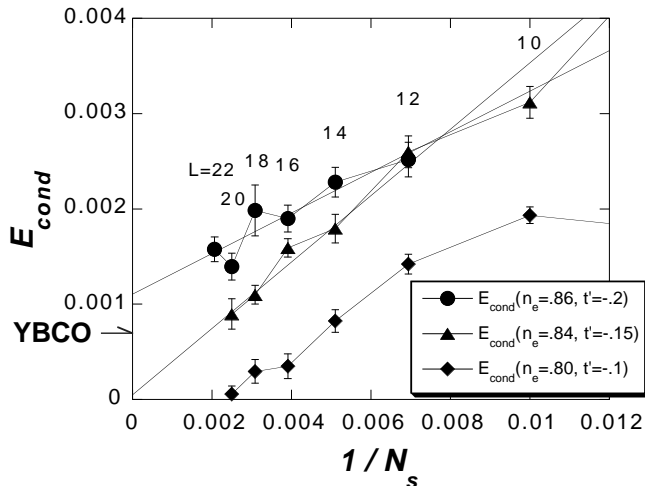


FIG. 5: Energy gain per site in the SC state with reference to the normal state for the 2D Hubbard model is plotted as a function of  $1/N$ .  $L$  is the length of the edge of the square lattice. YBCO attached to the vertical axis indicates the experimental value of the SC condensation energy for  $\text{YBa}_2\text{Cu}_3\text{O}_4$ . [97]

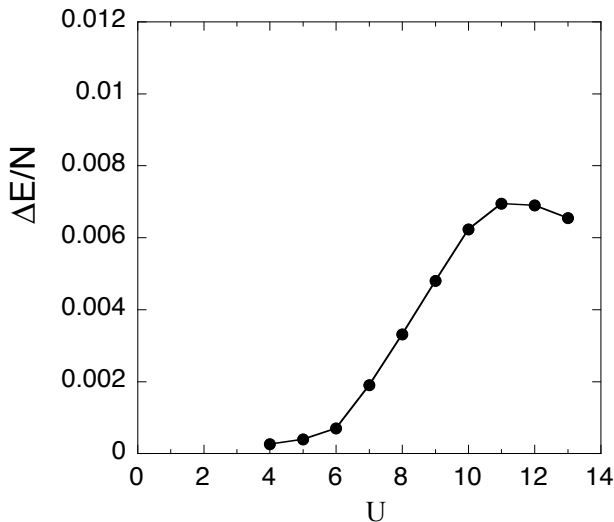


FIG. 6: Energy gain per site in the SC state with reference to the normal state for the 2D Hubbard model as a function of the Coulomb repulsion  $U$ . The system is  $10 \times 10$  with the electron number  $N_e = 84$  and  $t' = -0.3$ .

### B. Superconducting Condensation Energy

We study the cases of the  $d$ -, extended  $s$ - ( $s^*$ -) and  $s$ -wave gap functions in the following:

$$d \quad \Delta_{\mathbf{k}} = \Delta(\cos(k_x) - \cos(k_y)), \quad (26)$$

$$s^* \quad \Delta_{\mathbf{k}} = \Delta(\cos(k_x) + \cos(k_y)), \quad (27)$$

$$s \quad \Delta_{\mathbf{k}} = \Delta. \quad (28)$$

In Fig.4 calculated energies per site with  $N_e = 84$  on the  $10 \times 10$  lattice are shown for the case of  $U = 8$  and  $t' =$

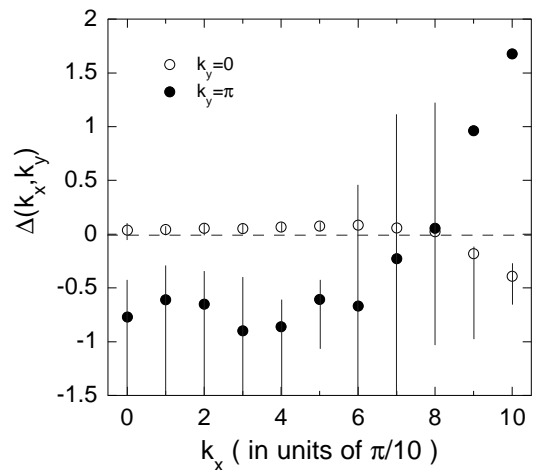


FIG. 7: The values of components of  $\Delta_{\mathbf{k}}$  for the two-chain Hubbard model. All the values of  $k_x$  of the bonding band ( $k_y = 0$ ) and antibonding band ( $k_y = \pi$ ) correspond to the energy minimum for  $20 \times 2$  lattice with 34 electrons. The parameters in the Hamiltonian are  $t_d = 1.8$  and  $U_0 = 8$  and the variational parameters are  $\mu = 0.0182$  and  $g = 0.415$ . [54]

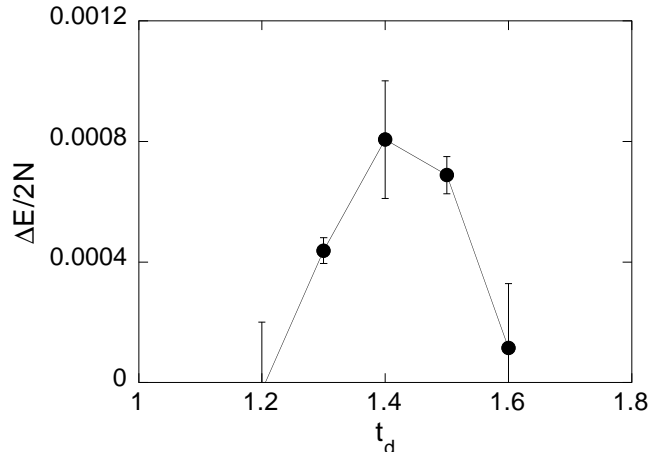


FIG. 8:  $t_d$  dependence of the SC condensation energy  $\Delta E/2N$  for the two-chain Hubbard model in the bulk limit. [54]

0. [46]  $E_g/N$  is plotted as a function of  $\Delta$  for three types of gap functions shown above. We impose the periodic and the antiperiodic boundary conditions for  $x$ - and  $y$ -direction, respectively. This set of boundary conditions is chosen so that  $\Delta_{\mathbf{k}}$  does not vanish for any  $\mathbf{k}$ -points occupied by electrons.  $E_g$  was obtained as the average of the results of several Monte Carlo calculations each with  $5 \times 10^7$  steps.  $E_g/N$  has minimum at a finite value of  $\Delta \simeq 0.08$  in the case of the  $d$ -wave gap function.

The energy gain  $\Delta E_g$  in the superconducting state is called the SC condensation energy in this paper.  $\Delta E_g/N$  is plotted as a function of  $1/N$  in Fig.5 in order to examine the size dependence of the SC energy gain. [97] Lattice sizes treated are from  $8 \times 8$  to  $22 \times 22$ . The electron density  $n_e$  is in the range of  $0.80 \geq n_e \leq 0.86$ . Other

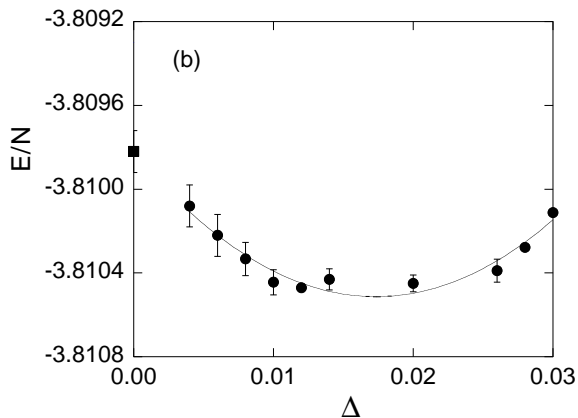
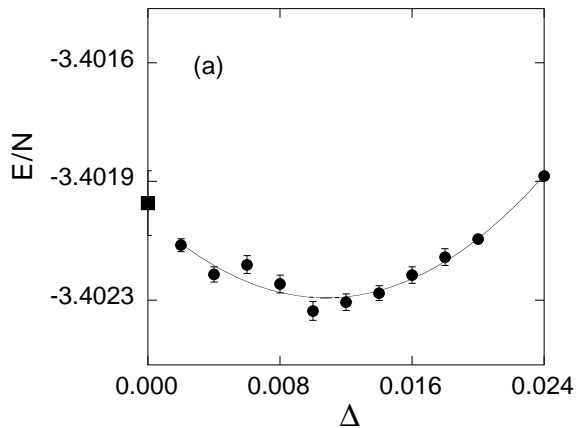


FIG. 9: Ground-state energy per site as a function of  $\Delta$  with the  $d$ -wave gap function for the three-band Hubbard model. The size of lattice is  $6 \times 6$ . Parameters are  $U = 8$ ,  $t_{pp} = 0$  and  $\epsilon_p - \epsilon_d = 2$  in units of  $t_{dp}$ . The doping rate is  $\delta = 0.111$  for (a) and  $\delta = 0.333$  for (b). Squares denote the energies for the normal-state wave function.[24]

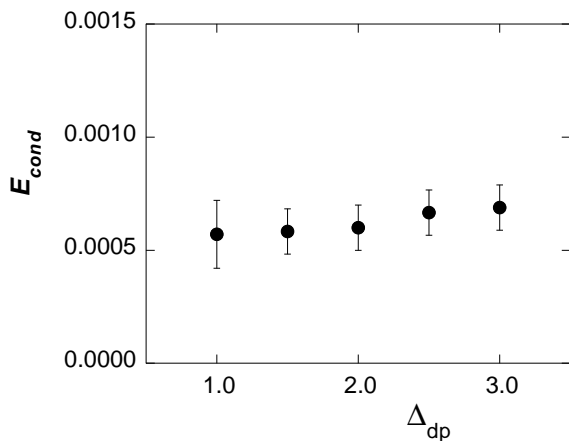


FIG. 10: Energy gain per site in the SC state as a function of the level difference  $\Delta_{dp} = \epsilon_p - \epsilon_d$  for the three-band Hubbard model with  $U_d = 8$  and  $t_{pp} = 0.2$ . [24] The size of lattice is  $6 \times 6$  sites.

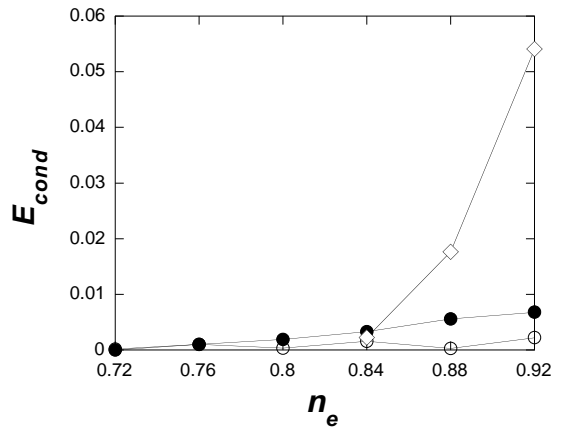


FIG. 11: Energy gain per site in the SDW state (diamonds) against electron density for  $t' = 0$  and the energy gain in the SC state for  $t' = 0$  (open circles) and  $t' = -0.1$  (solid circles). The model is the 2D Hubbard model on  $10 \times 10$  lattice.[46]

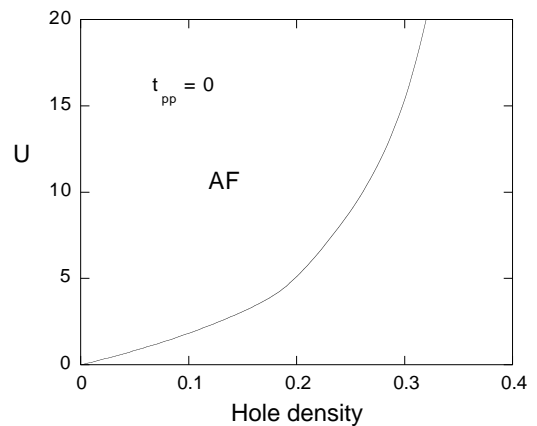


FIG. 12: Antiferromagnetic region in the plane of  $U$  and the hole density for  $t_{pp} = 0.0$  and  $\epsilon_p - \epsilon_d = 2$ .

parameters are  $-0.20 \leq t' \leq 0.0$  and  $U/t = 8$  in  $t$  units. Bulk limit  $N \rightarrow \infty$  of SC condensation energy  $E_{cond}$  was obtained by plotting as a function of  $1/N$ . The linear fitting line indicates very clearly that the bulk limit remains finite when  $-0.25 \leq t' \leq -0.10$  and  $n_e \geq 0.84$ . When  $n_e = 0.86$ ,  $t' = -0.20$  and  $U = 8$ , the bulk-limit  $E_{cond}$  is  $E_{cond} = 0.00117/\text{site} \simeq 0.60$  meV/site, where  $t = 0.51$  eV is used.[98] Thus the superconductivity is a real bulk property, not a spurious size effect. The value is remarkably close to experimental values  $0.17 \sim 0.26$  meV/site estimated from specific heat data[99, 100] and  $0.26$  meV/site from the critical magnetic field  $H_c$ [101] for optimally doped  $\text{YBa}_2\text{Cu}_3\text{O}_4$  (YBCO). This good agreement strongly indicates that the 2D Hubbard model includes essential ingredients for the superconductivity in the cuprates.

We just point out that the t-J model gives  $E_{cond} = 0.026t \simeq 13$  meV/site at  $n_e = 0.84$  for  $J = 4t^2/U = 0.5$

and  $t' = 0$ . [102] This value is 50 times larger than the experimental values indicating a serious quantitative problem with this model. This means that the t-J model made from the leading two terms in the expansion in terms of  $t/U$  of the canonical transformation of the Hubbard model should be treated with the higher-order terms in order to give a realistic SC condensation energy.

Here we show the SC condensation energy as a function of  $U$  in Fig.6. The condensation energy  $E_{cond} = \Delta E/N$  is increased as  $U/t$  is increased as far as  $U/t \leq 12$ . In the strong coupling region  $U > 8t$ , we obtain the large condensation energy.

### C. Fermi Surface and Condensation Energy

Now let us consider the relationship between the Fermi surface structure and the strength of superconductivity. The experimental SC condensation energy for  $(\text{La,Sr})_2\text{CuO}_4$  (LSCO) is estimated at  $0.029\text{meV}/(\text{Cu site})$  or  $0.00008$  in units of  $t$  which is much smaller than that for YBCO. [103] The band parameter values of LSCO were estimated as  $t' = -0.12$  and  $t'' = 0.08$ . [104] This set corresponds roughly to  $E_{cond} \simeq 0.0010$ . The latter value is much larger than the above-mentioned experimental value for LSCO. However, the stripe-type SDW state coexists with superconductivity [105, 106] and the SC part of the whole  $E_{cond}$  is much reduced. Therefore, such a coexistence allows us to qualitatively understand the SC  $E_{cond}$  in LSCO.

On the other hand, Tl2201 ( $T_c = 93\text{K}$ ) and Hg1201 ( $T_c = 98\text{K}$ ) band calculations by Singh and Pickett [107] give very much deformed Fermi surfaces that can be fitted by large  $|t'|$  such as  $t' \sim -0.4$ . For Tl2201, an Angular Magnetoresistance Oscillations (AMRO) work [108] gives information of the Fermi surface, which allows to get  $t' \sim -0.2$  and  $t'' \sim 0.165$ . There is also an Angle-Resolved Photoemission Study (ARPES) [109], which provides similar values. In the case of Hg1201, there is an ARPES work [110], from which we obtain by fitting  $t' \sim -0.2$  and  $t'' \sim 0.175$ . For such a deformed Fermi surface,  $E_{cond}$  in the bulk limit is reduced considerably. [111, 112] Therefore, the SC  $E_{cond}$  calculated by VMC indicates that the Fermi surface of LSCO-type is more favorable for high  $T_c$ . The lower  $T_c$  in LSCO may be attributed to the coexistence with antiferromagnetism of stripe type.

### D. Ladder Hubbard Model

The SC condensation energy in the bulk limit for the ladder Hubbard model has also been evaluated using the variational Monte Carlo method. [54] The Hamiltonian is given by the 1D two-chain Hubbard model: [51, 52, 55,

56, 85, 113–116]

$$\begin{aligned}
 H_{ladder} = & -t_d \sum_{\ell\sigma} (c_{1\ell\sigma}^\dagger c_{2\ell\sigma} + \text{h.c.}) \\
 & - t \sum_{j=1}^2 \sum_{\ell\sigma} (c_{j\ell\sigma}^\dagger c_{j,\ell+1,\sigma} + \text{h.c.}) \\
 & + U_0 \sum_{j=1}^2 \sum_{\ell} c_{j\ell\uparrow}^\dagger c_{j\ell\uparrow} c_{j\ell\downarrow}^\dagger c_{j\ell\downarrow}, \quad (29)
 \end{aligned}$$

where  $c_{j\ell\sigma}^\dagger$  ( $c_{j\ell\sigma}$ ) is the creation (annihilation) operator of an electron with spin  $\sigma$  at the  $\ell$ th site along the  $j$ th chain ( $j = 1, 2$ ).  $t$  is the intrachain nearest-neighbor transfer and  $t_d$  is the interchain nearest-neighbor transfer energy. The energy is measured in  $t$  units. The energy minimum was given when the components of the gap function  $\Delta_k$  take finite values plotted in Fig.7 for the lattice of  $20 \times 2$  sites with 34 electrons imposing the periodic boundary condition. [54] Each component of  $\Delta_k$  was optimized for  $U_0 = 8$  and  $t_d = 1.8$ . There are two characteristic features; one is that the components of the bonding and antibonding bands have opposite signs each other and second is that the absolute values of  $\Delta_k$  of the antibonding band ( $k_y = \pi$ ) is much larger than that of the bonding band ( $k_y = 0$ ). In order to reduce the computation cpu time,  $\Delta_k$  of each band was forced to take a fixed value specific to each band, i.e.  $\Delta_1$  for the bonding band and  $\Delta_2$  for the antibonding band. This drastically reduces the number of the variational parameters but still allows us to get a substantial value of the condensation energy.  $\Delta_1$  and  $\Delta_2$  take opposite sign, which is similar to that of the  $d_{x^2-y^2}$  gap function.

The energy gain  $\Delta F_{2c}$  remains finite in the bulk limit when  $1.2 < t_d < 1.6$ . The SC condensation energy per site in the bulk limit is plotted as a function of  $t_d$  in Fig.8. [54] The SC region derived from the SC condensation energy in the bulk limit is consistent with the results obtained from the density-matrix renormalization group [55, 56] and the exact-diagonalization method. [51, 52, 115] The maximum value of  $\Delta E_{2c}$  is  $0.0008$  which is of the same order of magnitude as the maximum condensation energy obtained for the 2D Hubbard model. [46]

### E. Condensation Energy in the d-p Model

The SC energy gain for the d-p model, namely, three-band Hubbard model in eq.(4) has also been evaluated using the variational Monte Carlo method. For the three-band model the wave functions are written as

$$\psi_n = P_G \prod_{|k| \leq k_F, \sigma} \alpha_{k\sigma}^\dagger |0\rangle, \quad (30)$$

$$\psi_{SC} = P_G P_{N_e} \prod_k (u_k + v_k \alpha_{k\uparrow}^\dagger \alpha_{-k\downarrow}^\dagger) |0\rangle, \quad (31)$$

where  $\alpha_{k\sigma}$  is the linear combination of  $d_{k\sigma}$ ,  $p_{xk\sigma}$  and  $p_{yk\sigma}$  constructed to express the operator for the lowest band (in the hole picture) or the highest band (in the electron picture) of the non-interacting Hamiltonian. The numerical calculations have been done in the hole picture. The Gutzwiller parameter  $g$ , effective level difference  $\tilde{\epsilon}_p - \tilde{\epsilon}_d$ , chemical potential  $\mu$  and superconducting order parameter  $\Delta$  are the variational parameters.

The similar results to the single-band Hubbard model were obtained as shown in Fig.9 for  $t_{pp} = 0.0$ ,  $U_d = 8$  and  $\epsilon_d - \epsilon_p = 2$  in  $t_{dp}$  units where the calculations were performed in the hole picture.[24] The SC condensation energy for the three-band model is  $E_{cond} \simeq 0.0005t_{dp} \simeq 0.75$  meV per site in the optimally doped region. We set  $t_{dp} = 1.5$  eV as estimated in Table I. There is a tendency that  $E_{cond}$  increases as  $\epsilon_d - \epsilon_p$  increases which is plotted in Fig.10. This tendency is not, however, in accordance with NQR (nuclear quadrupole resonance) study on cuprates.[117] We think that the NQR experiments indicate an importance of the Coulomb interaction on oxygen sites. This will be discussed in section III.K.

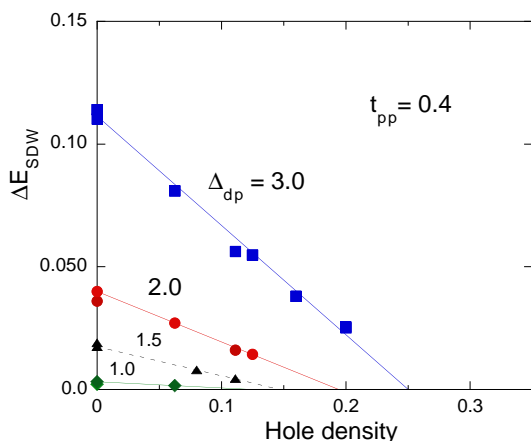


FIG. 13: Energy gain per site  $(E_{normal} - E)/N$  in the SDW state as a function of hole density  $\delta$  for the three-band Hubbard model. Parameters are  $t_{pp} = 0.4$  and  $U_d = 8$  in  $t_{dp}$  units. From the top,  $\Delta_{dp} \equiv \epsilon_p - \epsilon_d = 3, 2, 1.5$  and  $1$ . The results are for  $6 \times 6, 8 \times 8, 10 \times 10$  and  $16 \times 12$  systems. Antiperiodic and periodic boundary conditions are imposed in  $x$ - and  $y$ -direction, respectively. Monte Carlo statistical errors are smaller than the size of symbols. Curves are a guide to the eye.[24]

## F. Antiferromagnetic State

When the density of doped holes is zero or small, the 2D single-band or three-band Hubbard model takes an antiferromagnetic state as its ground state. The magnetic order is destroyed and superconductivity appears with the increase of doped hole density. The transition between the  $d$ -wave SC and the uniform SDW states has been investigated by computing the energy of the SDW

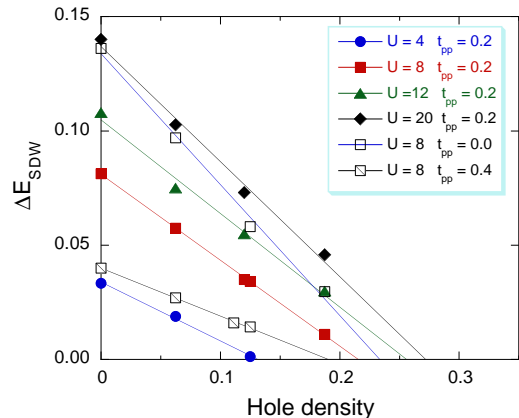


FIG. 14: Uniform SDW energy gain per site with reference to the normal-state energy as a function of the hole density for the three-band Hubbard model. Data are from  $8 \times 8, 10 \times 10, 12 \times 12$  and  $16 \times 12$  systems for  $\epsilon_p - \epsilon_d = 2$ . For solid symbols  $U_d = 4$  (circles),  $U_d = 8$  (squares),  $U_d = 12$  (triangles) and  $U_d = 20$  (diamonds) for  $t_{pp} = 0.2$ . For open symbols  $U_d = 8$  and  $t_{pp} = 0$ , and for open squares with slash  $U_d = 8$  and  $t_{pp} = 0.4$ . The lines are a guide to the eye. The Monte Carlo statistical errors are smaller than the size of symbols.[47]

state by using the variational Monte Carlo method. The trial SDW wave function is written as

$$\psi_{AF} = P_G \psi_{SDW}, \quad (32)$$

$$\begin{aligned} \psi_{SDW} = & \prod_{\mathbf{k}} (u_{\mathbf{k}} c_{\mathbf{k}\uparrow}^\dagger + v_{\mathbf{k}} c_{\mathbf{k}+Q\uparrow}^\dagger) \\ & \times \prod_{\mathbf{k}'} (u_{\mathbf{k}'} c_{\mathbf{k}'\downarrow}^\dagger - v_{\mathbf{k}'} c_{\mathbf{k}'+Q\downarrow}^\dagger) |0\rangle, \end{aligned} \quad (33)$$

$$u_{\mathbf{k}} = [(1 - w_{\mathbf{k}} / (w_{\mathbf{k}}^2 + \Delta_{AF}^2)^{1/2}) / 2]^{1/2}, \quad (34)$$

$$v_{\mathbf{k}} = [(1 + w_{\mathbf{k}} / (w_{\mathbf{k}}^2 + \Delta_{AF}^2)^{1/2}) / 2]^{1/2}, \quad (35)$$

$$w_{\mathbf{k}} = (\epsilon_{\mathbf{k}} - \epsilon_{\mathbf{k}+Q}) / 2. \quad (36)$$

Summation over  $\mathbf{k}$  and  $\mathbf{k}'$  in eq.(33) is performed over the filled  $\mathbf{k}$ -points, as in the calculation of the normal state energy.  $Q$  is the SDW wave vector given by  $(\pi, \pi)$  and  $\Delta_{AF}$  is the SDW potential amplitude.

As shown in Fig.11, the energy gain per site in the SDW state rises very sharply from  $n_e \sim 0.84$  for  $t' = 0$ . [46] At  $n_e \sim 0.84$  it is slightly larger than that in the SC state, and at  $n_e = 0.80$  there is no more stable SDW state. Thus the boundary between the SDW and the SC states is given at  $n_e \sim 0.84$ . The results of the bulk limit calculations indicate that the energy gain in the SC state at  $n_e = 0.84$  takes the extremely small value and the value at  $n_e = 0.80$  vanishes as  $N \rightarrow 0$ . Hence the pure  $d$ -wave SC state possibly exists near the boundary at  $n_e \sim 0.84$ , but the region of pure SC state is very restricted.

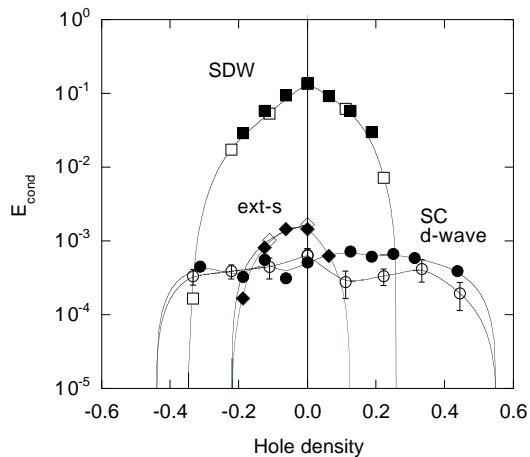


FIG. 15: Condensation energy per site as a function of hole density for the three-band Hubbard model where  $t_{pp} = 0.0$ ,  $\epsilon_p - \epsilon_d = 2$  and  $U_d = 8$ . Circles and squares denote the energy gain per site with reference to the normal-state energy for  $d$ -wave, ext- $s$  wave and SDW states, respectively. For extremely small doping rate, the extended  $s$ -wave state is more favorable than the  $d$ -wave state. Solid symbols are for  $8 \times 8$  and open symbols are for  $6 \times 6$ . Curves are a guide to the eye.

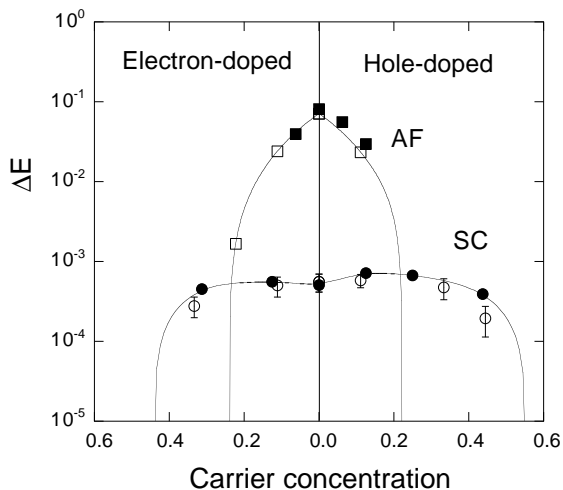


FIG. 16: Condensation energy per site as a function of hole density for the three-band Hubbard model where  $t_{pp} = 0.2$ ,  $\epsilon_p - \epsilon_d = 2$  and  $U_d = 8$ . Circles and squares denote the energy gain per site with reference to the normal-state energy for  $d$ -wave and SDW states, respectively. Solid symbols are for  $8 \times 8$  and open symbols are for  $6 \times 6$ . Curves are a guide to the eye.

Let us turn to the three-band model. We show the antiferromagnetic-paramagnetic boundary for  $t_{pp} = 0.0$  and  $\epsilon_p - \epsilon_d = 2$  in the plane of  $U$  and the hole density in Fig.12 where AF denotes the antiferromagnetic region.[47] The value  $\epsilon_p - \epsilon_d = 2$  is taken from the estimations by cluster calculations.[89–91] The phase boundary

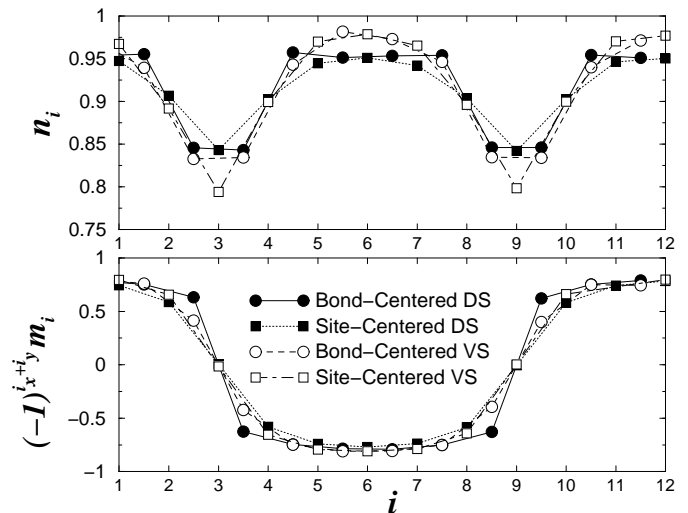


FIG. 17: Charge and spin density as a function of the distance for a striped state.[50]

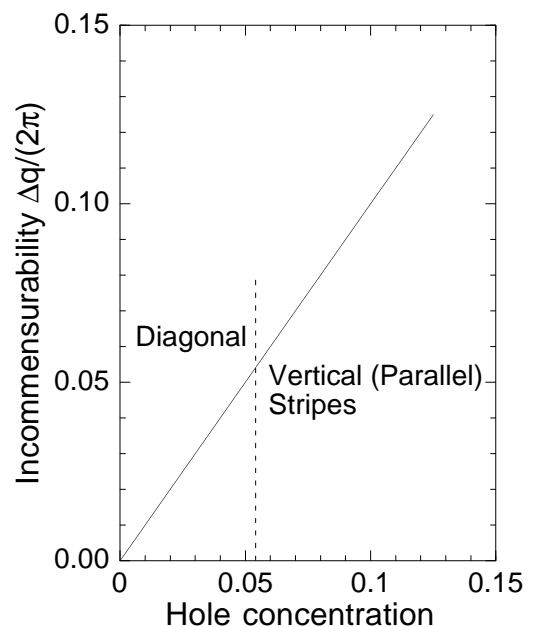


FIG. 18: Schematic illustration of the incommensurability versus hole density.

in the region of small  $U$  is drawn from an extrapolation. For the intermediate values of  $U \sim 8 - 12$ , the antiferromagnetic long-range ordering exists up to about 20 percent doping. Thus the similar features are observed compared to the single-band Hubbard model.

Since the three-band Hubbard model contains several parameters, we must examine the parameter dependence of the energy of SDW state. The energy gain  $\Delta E_{SDW}$  in the SDW state is shown in Fig.13 as a function of doping ratio for several values of  $\Delta_{dp} \equiv \epsilon_p - \epsilon_d$ .  $\Delta E_{SDW}$  increases as  $\Delta_{dp}$  increases as expected. In Fig.14  $t_{pp}$ - and

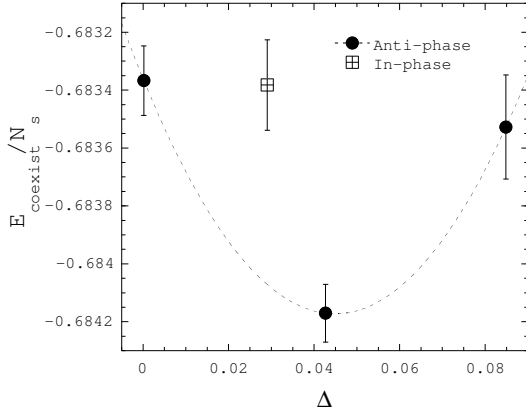


FIG. 19: Coexistent state energy per site  $E_{coexist}/N_s$  versus  $\Delta$  for the case of 84 electrons on  $12 \times 8$  sites with  $U = 8$  and  $t' = -0.2$ . Here the vertical stripe state has 8-lattice periodicity for the hole density  $p = 0.125$ . Only  $E_{coexist}/N_s$  for the optimized gap is plotted for the in-phase superconductivity.

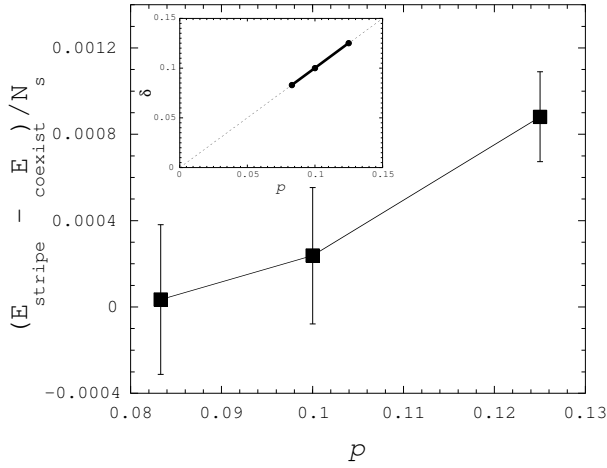


FIG. 20: Superconducting condensation energy per site in the coexistence state as a function of the hole density  $p = 0.0833, 0.10$  and  $0.125$ . The model is the single-band Hubbard Hamiltonian with  $t' = -0.20$ . The stripe interval is preserved constant. The inset shows the hole dependence of the incommensurability in the coexistent state.[105]

$U_d$ -dependencies of  $\Delta E_{SDW}$  are presented. The SDW phase extends up to 30 percent doping when  $U_d$  is large. It follows from the calculations that the SDW region will be reduced if  $\epsilon_p - \epsilon_d$  and  $U_d$  decrease.

From the calculations for the SDW wave functions, we should set  $\epsilon_p - \epsilon_d$  and  $U_d$  small so that the SDW phase does not occupy a huge region near half-filling. In Figs.15 and 16 we show energy gains for both the SDW and SC states for  $U_d = 8$ ,  $t_{pp} = 0, 0.2$  and  $\epsilon_p - \epsilon_d = 2$ , where the right hand side and left hand side indicate the hole-doped and electron-doped case, respectively. Solid symbols indicate the results for  $8 \times 8$  and open symbols for  $6 \times 6$ . For this set of parameters the SDW region extends up to 20 percent doping and the pure  $d$ -wave phase exists outside

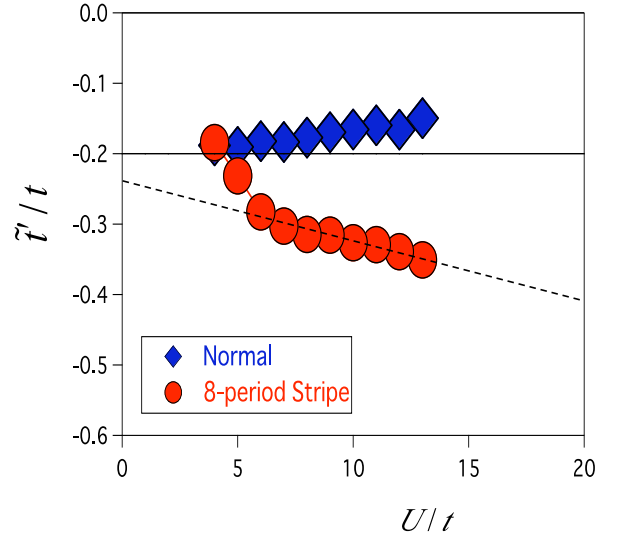


FIG. 21: Optimized effective second neighbor transfer energy  $\tilde{t}'/t$  as a function of  $U/t$ . The system is a  $16 \times 16$  lattice with  $t'/t = -0.2$  and the electron density 0.875

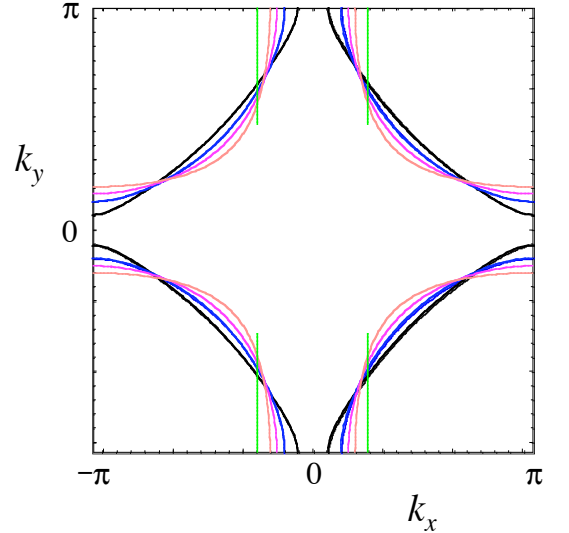


FIG. 22: Renormalized quasi-Fermi surface for  $\tilde{t}'/t = -0.3, -0.4$  and  $-0.5$ . The system is the same as that in Fig.21.

of the SDW phase. The  $d$ -wave phase may be possibly identified with superconducting phase in the overdoped region in the high- $T_c$  superconductors.

### G. Stripes and its Coexistence with Superconductivity

Incommensurate magnetic and charge peaks have been observed from the elastic neutron-scattering experiments in the underdoped region of the Nd-doped  $\text{La}_{2-x-y}\text{Nd}_y\text{Sr}_x\text{CuO}_4$ . [118] (Fig.17) Recent neutron experiments have also revealed the incommensurate spin structures.[119–123] Rapid decrease of the Hall resist-

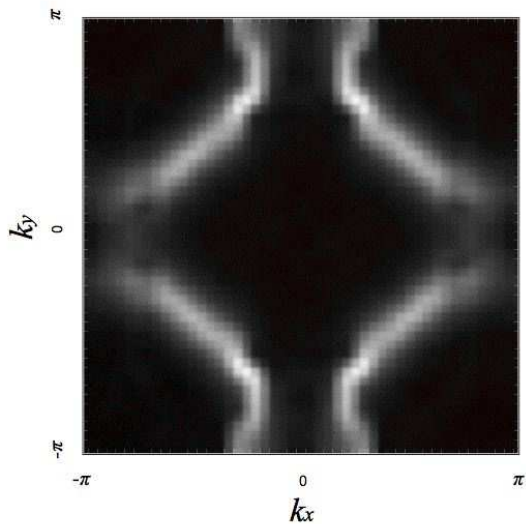


FIG. 23: Contour plot of  $|\nabla n_k|$  measured for the projected stripe state on  $24 \times 24$  lattice with  $t'/t = -0.2$ . The electron density is 0.875.

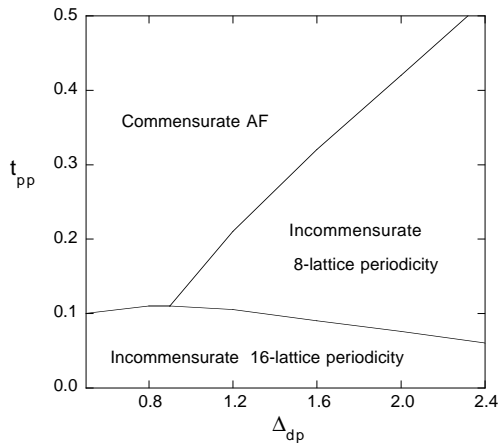


FIG. 24: Phase diagram of stable antiferromagnetic state in the plane of  $\Delta_{dp} = \epsilon_p - \epsilon_d$  and  $t_{pp}$  obtained for  $16 \times 4$  lattice.

tivity in this region suggests that the electric conduction is approximately one dimensional.[124] The angle-resolved photo-emission spectroscopy measurements also suggested a formation of two sets of one-dimensional Fermi surface.[125] Then it has been proposed that these results might be understood in the framework of the stripe state where holes are doped in the domain wall between the undoped spin-density-wave domains. This state is a kind of incommensurate SDW state. It was also shown that the incommensurability is proportional to the hole density in the low-doping region in which the hole number per stripe is half of the site number along one stripe.[118, 120] A static magnetically ordered phase has been observed by  $\mu$ SR over a wide range of SC phase for  $0.05 < x < 0.1$  in  $\text{La}_{2-x}\text{Sr}_x\text{CuO}_4$  (LSCO).[126] Thus the

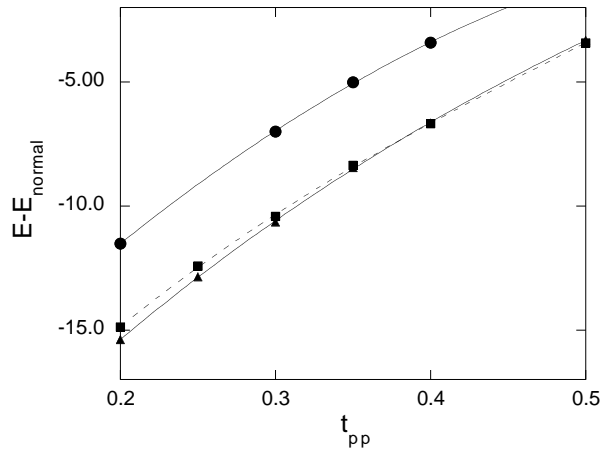


FIG. 25: Energy as a function of  $t_{pp}$  for  $16 \times 16$  square lattice at  $x = 1/16$ . Circles, triangles and squares denote the energy for 4-lattice stripes, 8-lattice stripes, and commensurate SDW, respectively, where  $n$ -lattice stripe is the incommensurate state with one stripe per  $n$  ladders. The boundary conditions are antiperiodic in  $x$ -direction and periodic in  $y$ -direction.[47, 106]

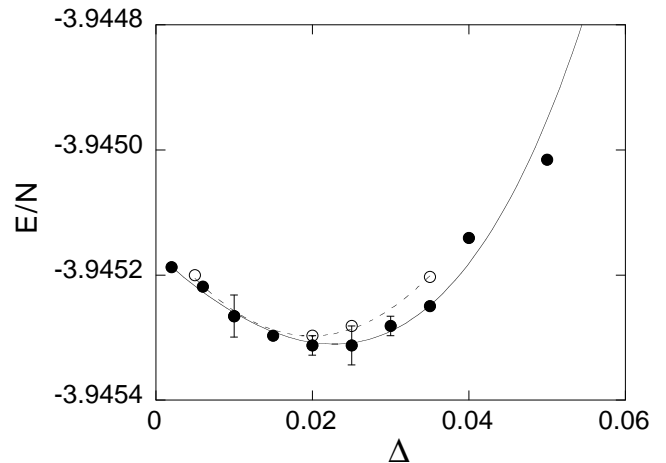


FIG. 26: Energy of the coexistent state as a function of the SC order parameter for  $x = 0.125$  on  $16 \times 4$  lattice. We assume the incommensurate antiferromagnetic order (stripe). Parameters are  $\epsilon_p = 0$ ,  $\epsilon_d = -2$ ,  $t_{pp} = 0.4$  and  $U_d = 8$  in  $t_{dp}$  units. For solid circles the SC gap function is taken as  $\Delta_{i,i+\hat{x}} = \Delta \cos(Q_x(x_i + \hat{x}/2))$  and  $\Delta_{i,i+\hat{y}} = -\Delta \cos(Q_x(x_i))$ , while for the open circles  $\Delta_{i,i+\hat{x}} = \Delta \cos|Q_x(x_i + \hat{x}/2)|$  and  $\Delta_{i,i+\hat{y}} = -\Delta |\cos(Q_x(x_i))|$ .  $Q_x = 2\pi\delta = \pi/4$ .

possibility of superconductivity that occurs in the stripe state is a subject of great interest.[127–130] The incommensurate magnetic scattering spots around  $(\pi, \pi)$  were observed in the SC phase in the range of  $0.05 < x < 0.13$  in the elastic and inelastic neutron-scattering experiments with LSCO.[127, 128, 130] The hole dependence of the incommensurability and the configuration of the spots around the Bragg spot in the SC phase indicated the vertical stripe. The neutron-scattering experiments

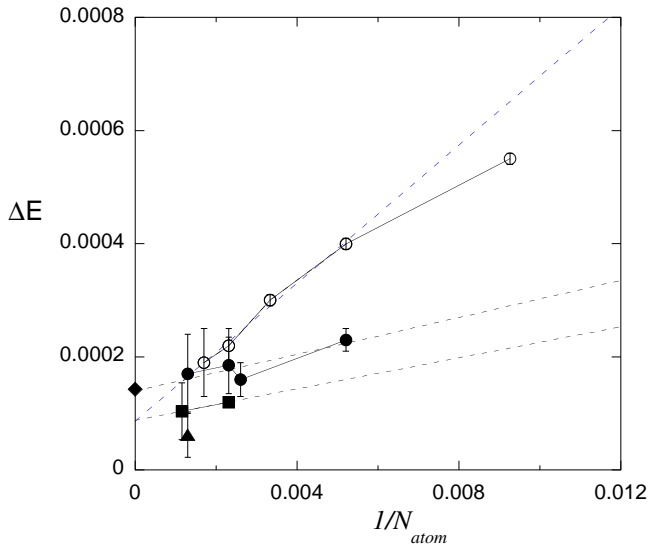


FIG. 27: Energy gain due to the SC order parameter as a function of the system size  $N_{atom} = 3N_s$ . Parameters are  $\epsilon_p = 0$ ,  $\epsilon_d = -2$ ,  $t_{pp} = 0.4$  and  $U_d = 8$ . The open circle is for the simple  $d$ -wave pairing at the hole density  $x = 0.2$ . The solid symbols indicate the energy gain of the coexistent state; the solid circle is at  $x = 0.125$ , the solid square is at  $x = 0.08333$  and the solid triangle is at  $x = 0.0625$ . The diamond shows the SC condensation energy obtained on the basis of specific heat measurements[99].

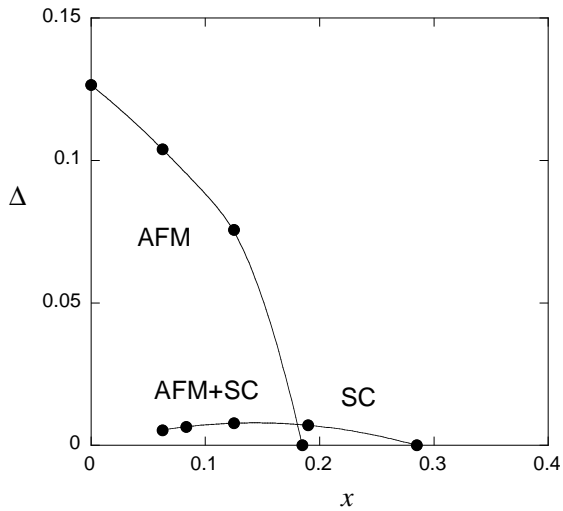


FIG. 28: Phase diagram of the d-p model based on the Gutzwiller wave function.[106]

have also revealed that a diagonal spin modulation occurs across the insulating spin-glass phase in  $\text{La}_{2-x}\text{Sr}_x\text{CuO}_4$  for  $0.02 \leq x \leq 0.05$ , where a one-dimensional modulation is rotated by 45 degrees from the stripe in the SC phase. The incommensurability  $\delta$  versus hole density is shown in Fig.18 schematically.[129, 130] The diagonal stripe changes into the vertical stripe across the boundary between the insulating and SC phase.

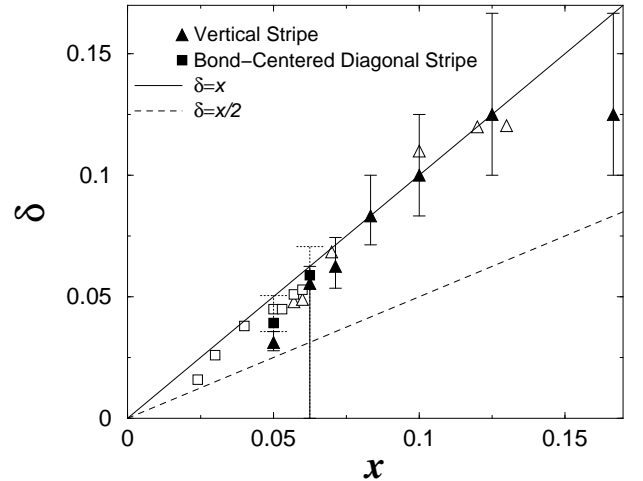


FIG. 29: Incommensurability  $\delta$  as a function of the hole density  $x$  for  $U = 8$  and  $t' = -0.2$ . [50] The numerical results for the vertical and the bond-centered diagonal stripe state are represented by solid triangles and square symbols, respectively. Open triangles and squares show the results of the vertical and diagonal incommensurate SDW order observed from neutron scattering measurements, respectively.[130]

Let us investigate the doped system from the point of modulated spin structures.[131–141] The stripe SDW state has been studied theoretically by using the mean-field theory.[132–136] They found that the stripe state appears when an incommensurate nesting becomes favorable in the hole-doped 2D Hubbard model. When the electron correlation correlation is strong or intermediate, it was shown that the stripe state is more stable than the commensurate spin-density-wave state with the wave vector  $(\pi, \pi)$  in the ground state of the 2D Hubbard model by using the variational Monte Carlo method.[131] It has also been confirmed by the same means that the stripe states are stabilized in the d-p model.[48] The purpose of this section is to examine whether the superconductivity can coexist with static stripes in the 2D Hubbard model in a wider doping region and investigate the doping dependence of the coexisting state.

We consider the 2D Hubbard model on a square lattice. We calculate the variational energy in the coexistent state that is defined by

$$\psi_{coexist} = P_{N_e} P_G \phi_{coexist}^{MF}, \quad (37)$$

where  $\phi_{coexist}^{MF}$  is a mean-field wave function. The effective mean-field Hamiltonian for the coexisting state is [105] represented by

$$H_{MF} = \sum_{ij} (c_{i\uparrow}^\dagger c_{i\downarrow}) \begin{pmatrix} H_{ij\uparrow} & F_{ij} \\ F_{ji}^* & -H_{ji\downarrow} \end{pmatrix} \begin{pmatrix} c_{j\uparrow} \\ c_{j\downarrow} \end{pmatrix}, \quad (38)$$

where the diagonal terms describe the incommensurate spin-density wave state:

$$H_{ij\sigma} = -t_{ij} - \mu + \frac{U}{2} [n_i + \text{sign}(\sigma)(-1)^{x_i+y_i} m_i] \delta_{ij}, \quad (39)$$

where  $\mu$  is the chemical potential. The vertical stripe state is represented by the charge density  $n_i$  and the spin density  $m_i$  that are spatially modulated as

$$n_i = 1 - \sum_{\ell} \alpha / \cosh \left( \frac{y_i - Y_{\ell}}{\xi_c} \right), \quad (40)$$

$$m_i = m \prod_{\ell} \tanh \left( \frac{y_i - Y_{\ell}}{\xi_c} \right), \quad (41)$$

where  $Y_{\ell}$  denotes the position of vertical stripes. The amplitude  $\alpha$  is fixed by  $\sum_i n_i = N_e$ . The off-diagonal terms in eq.(38) are defined in terms of the  $d$ -wave SC gap as

$$F_{ij} = \sum_{\hat{e}} \Delta_{ij} \delta_{j+i\hat{e}}, \quad (42)$$

where  $\hat{e} = \pm\hat{x}, \pm\hat{y}$  (unit vectors). We consider two types of the spatially inhomogeneous superconductivity: anti-phase and in-phase defined as

$$\Delta_{i,i+\hat{x}} = \Delta \cos(q_y(y_i - Y)), \quad (43)$$

$$\Delta_{i,i+\hat{y}} = -\Delta \cos(q_y(y_i - Y + \hat{y}/2)), \quad (44)$$

and

$$\Delta_{i,i+\hat{x}} = \Delta |\cos(q_y(y_i - Y))|, \quad (45)$$

$$\Delta_{i,i+\hat{y}} = -\Delta |\cos(q_y(y_i - Y + \hat{y}/2))|, \quad (46)$$

respectively. Here,  $\mathbf{q} = (0, 2\pi\delta)$  and  $\delta$  is a incommensurability given by the stripe's periodicity in the  $y$  direction with regard to the spin. The anti-phase (in-phase) means that the sign of the superconducting gap is (is not) changed between nearest domain walls.

The wave function  $\psi_{coexist}^0$  is made from the solution of the Bogoliubov-de Gennes equation represented by

$$\sum_j (H_{ij\uparrow} u_j^{\lambda} + F_{ij} v_j^{\lambda}) = E^{\lambda} u_i^{\lambda}, \quad (47)$$

$$\sum_j (F_{ji}^* u_j^{\lambda} - H_{ji\downarrow} v_j^{\lambda}) = E^{\lambda} v_i^{\lambda}. \quad (48)$$

The Bogoliubov quasiparticle operators are written in the form

$$\alpha_{\lambda} = \sum_i (u_i^{\lambda} c_{i\uparrow} + v_i^{\lambda} c_{i\downarrow}^{\dagger}) \quad (E^{\lambda} > 0), \quad (49)$$

$$\alpha_{\bar{\lambda}} = \sum_i (u_i^{\bar{\lambda}} c_{i\uparrow} + v_i^{\bar{\lambda}} c_{i\downarrow}^{\dagger}) \quad (E^{\bar{\lambda}} < 0). \quad (50)$$

Then the coexistence wave function is written as[105, 142]

$$\begin{aligned} \psi_{coexist}^0 &= P_{N_e} \prod_{\lambda} \alpha_{\lambda} \alpha_{\bar{\lambda}}^{\dagger} |0\rangle \\ &= C P_{N_e} \exp \left( - \sum_{ij} (U^{-1}V)_{ij} c_{i\uparrow}^{\dagger} c_{j\downarrow}^{\dagger} \right) |0\rangle \\ &= C' \left( \sum_{ij} (U^{-1}V)_{ij} c_{i\uparrow}^{\dagger} c_{j\downarrow}^{\dagger} \right)^{N_e/2} |0\rangle, \quad (51) \end{aligned}$$

for constants  $C$  and  $C'$ . The calculations are performed for the wave function  $\psi_{coexist} = P_G \psi_{coexist}^0$ . The variational parameters are  $\mu, m, g, \xi_c$  and  $\xi_s$ . The system parameters were chosen as  $t' = -0.2$  and  $U = 8$  suitable for cuprate superconductors. It has been shown that the "anti-phase" configuration is more stable than the "in-phase" one.[105]

Here, the system parameters are  $t' = -0.2$  and  $U = 8$ . We use the periodic boundary condition in the  $x$ -direction and anti-periodic one in the  $y$ -direction. In Fig.19, we show the total energy of the coexistent state,  $E_{coexist}$ , as a function of the SC gap  $\Delta$  for the cases of anti-phase and in-phase. The SC condensation energy  $\Delta E_{coexist}$  is estimated as  $0.0008t$  per site at the hole density 0.125 on the  $12 \times 8$  lattice with periodic boundary condition in  $x$ -direction and antiperiodic one in  $y$ -direction.  $\Delta E_{coexist}$  in the coexistence state is defined as the decrease of energy due to finite  $\Delta$ . If we use  $t \sim 0.5\text{eV}$ , this is evaluated as  $\sim 0.4\text{meV}$ . The SC condensation energy per site is shown as a function of hole density in Fig.20. One finds that  $\Delta E_{coexist}$  in the stripe state decreases as the hole density decreases. This tendency is reasonable since the SC order is weakened in the domain of the incommensurate SDW because of the vanishingly small carrier concentration contributing the superconductivity in this domain. This behavior is consistent with the SC condensation energy estimated from the specific heat measurements.[143]

There is a large renormalization of the Fermi surface due to the correlation effect in the striped state.[144] We considered the next-nearest transfer  $t'$  in the trial function as a variational parameter  $\tilde{t}'$ . In Fig.21, optimized values of  $\tilde{t}'/t$  for the striped state are shown as a function of  $U/t$ . The  $\tilde{t}'/t$  increases as  $U/t$  increases. We also mention that the optimized  $t''/t$  almost vanishes. The renormalized Fermi surface of  $\tilde{t}'/t = -0.30, -0.40$  and  $-0.50$  are plotted in Fig.22. The system is a  $16 \times 16$  lattice with  $t'/t = -0.2$  and the electron density 0.875. As  $U/t$  is increased, the Fermi surface is more deformed. We show the gradient of the momentum distribution function,  $|\nabla n_k|$ , calculated in the optimized stripe state in Fig.23. The brighter areas coincide with the renormalized Fermi surface with  $\tilde{t}'/t = -0.31$  and  $\tilde{t}''/t = 0.0$  for  $U/t = 8$ .

The calculations for the three-band Hubbard model has also been done taking into account the coexistence of stripes and SC.[15, 106] The energy of antiferromagnetic state would be lowered further if we consider the incommensurate spin correlation in the wave function. The phase diagram in Fig.24 presents the region of stable AF phase in the plane of  $t_{pp}$  and  $\Delta_{dp} = \epsilon_p - \epsilon_d$ . For large  $\Delta_{dp} = \epsilon_p - \epsilon_d$ , we have the region of the AF state with an eight-lattice periodicity in accordance with the results of neutron-scattering measurements[118, 123]. The energy at  $x = 1/16$  is shown in Fig.25 where the 4-lattice stripe state has higher energy than that for 8-lattice stripe for all the values of  $t_{pp}$ .

The Bogoliubov-de Gennes equation is extended to the

case of three orbitals  $d$ ,  $p_x$  and  $p_y$ . ( $H_{ij\sigma}$ ) and ( $F_{ij}$ ) are now  $3N \times 3N$  matrices. The energy of the state with double order parameters  $\Delta$  and  $m$  is shown in Fig.26 on the  $16 \times 4$  lattice at the doping rate  $1/8$ . The SC condensation energy per site is evaluated as  $\sim 0.00016t_{dp}$  for  $U_d = 8$ ,  $t_{pp} = 0.4$  and  $\epsilon_p - \epsilon_d = 2$ . If we use  $t_{dp} \sim 1.5eV$ , [89–91] we obtain  $\Delta E_{coexist} \sim 0.24meV$  which is slightly smaller than and close to the value obtained for the single-band Hubbard model. We show the size dependence of the SC condensation energy for  $x = 0.2, 0.125, 0.08333$  and  $0.0625$  in Fig.27. We set the parameters as  $\epsilon_p - \epsilon_d = 2$  and  $t_{pp} = 0.4$  in  $t_{dp}$  units, which is reasonable from the viewpoint of the density of states and is remarkably in accordance with cluster estimations [89–91], and also in the region of eight-lattice periodicity at  $x = 1/8$ . We have carried out the Monte Carlo calculations up to  $16 \times 16$  sites (768 atoms in total). In the overdoped region in the range of  $0.18 < x < 0.28$ , we have the uniform  $d$ -wave pairing state as the ground state. The periodicity of spatial variation increases as the doping rate  $x$  decreases proportional to  $1/x$ . In the figure we have the 12-lattice periodicity at  $x = 0.08333$  and 16-lattice periodicity at  $x = 0.0625$ . For  $x = 0.2, 0.125$  and  $0.08333$ , the results strongly suggest a finite condensation energy in the bulk limit. The SC condensation energy obtained on the basis of specific heat measurements agrees well with the variational Monte Carlo computations [99]. In general, the Monte Carlo statistical errors are much larger than those for the single-band Hubbard model. The large number of Monte Carlo steps (more than  $5.0 \times 10^7$ ) is required to get convergent expectation values for each set of parameters.

In Fig.28 the order parameters  $\Delta_{AF}$  and  $\Delta_{SC}$  were evaluated using the formula  $E_{cond} = (1/2)N(0)\Delta^2$  where  $N(0)$  is the density of states. Here we have set  $N(0) \sim 5/t_{dp}$  since  $N(0)$  is estimated as  $N(0) \sim 2$  to  $3$  ( $eV$ ) $^{-1}$  for optimally doped YBCO using  $N(0)(k_B T_c)^2/2$  [100]. The phase diagram is consistent with the recently reported phase diagram for layered cuprates [145].

### H. Diagonal Stripe States in the Light-Doping Region

Here we examine whether the relationship  $\delta \sim x$  holds in the lower doping region or not, and whether the diagonal stripe state is obtained in the further lower doping region. [50] The elastic neutron scattering experiments of LSCO in the light-doping region,  $0.03 < x < 0.07$ , revealed that the position of incommensurate magnetic peaks changed from  $(1/2, 1/2 \pm \delta)$  to  $(1/2 \pm \delta', 1/2 \pm \delta')$  as  $x$  becomes less than  $0.06$ . [129, 130] This means that the stripe direction rotates by 45 degrees to become diagonal at this transition. In the diagonal stripe states, the magnetic peaks are observed to keep a relation  $\delta \sim x$  that holds in the vertical stripe state in the low doping region.

In Fig.29, we show the incommensurability of the most stable stripe state as a function of  $x$ . Open squares and

triangles are values for diagonal and vertical incommensurate SDW's obtained in the elastic neutron scattering experiments on LSCO, respectively. Solid squares and triangles show our results for the diagonal and vertical stripes, respectively. These results are in a good agreement with experimental data. We also found that the phase boundary  $x_{critical}$  between the diagonal and vertical stripe states lies at or above  $0.0625$  in the case of  $U = 8$  and  $t' = -0.2$ . The following factors may give rise to slight changes of the phase boundary  $x_{critical}$ : the diagonal stripe state may be stabilized in the low-temperature-orthorhombic (LTO) phase in LSCO. The diagonal stripe state is probably stabilized further by forming a line along larger next-nearest hopping direction due to the anisotropic  $t'$  generated by the Cu-O buckling in the LTO phase.

### I. Checkerboard States

A checkerboard-like density modulation with a roughly  $4a \times 4a$  period ( $a$  is a lattice constant) has also been observed by scanning tunneling microscopy (STM) experiments in  $Bi_2Sr_2CaCu_2O_{8+\delta}$ , [146]  $Bi_2Sr_{2-x}La_xCuO_{6+\delta}$ , [147] and  $Ca_{2-x}Na_xCuO_2Cl_2$  (Na-CCOC) [148]. It is important to clarify whether these inhomogeneous states can be understood within the framework of strongly correlated electrons.

Possible several electronic checkerboard states have been proposed theoretically. [134, 149, 150] The charge density  $\rho_i$  and spin density  $m_i$  are spatially modulated as

$$\rho_i = \sum_{\ell} \rho_{\ell} \cos(Q_{\ell}^c \cdot (\mathbf{r}_i - \mathbf{r}_0)), \quad (52)$$

$$m_i = \sum_{\ell} m_{\ell} \cos(Q_{\ell}^s \cdot (\mathbf{r}_i - \mathbf{r}_0)). \quad (53)$$

where  $\rho_{\ell}$  and  $m_{\ell}$  are variational parameters. The striped incommensurate spin-density wave state (ISDW) is defined by a single Q vector. On the other hand, the checkerboard ISDW state is described by the double-Q set; for example, vertical wave vectors  $Q_1^s = (\pi, \pi \pm 2\pi\delta)$  and  $Q_2^s = (\pi \pm 2\pi\delta, \pi)$  describe a spin vertical checkerboard state, where two diagonal domain walls are orthogonal. Diagonal wave vectors  $Q_1^s = (\pi \pm 2\pi\delta, \pi \pm 2\pi\delta)$  and  $Q_2^s = (\pi \pm 2\pi\delta, \pi \mp 2\pi\delta)$  lead to a spin diagonal checkerboard state with a  $1/\delta$ -period. The hole density forms the charge vertical checkerboard pattern with vertical wave vectors  $Q_1^c = (0, \pm 4\pi\delta)$  and  $Q_2^c = (2\pi \pm 4\pi\delta, 2\pi)$  in which the hole density is maximal on the crossing point of magnetic domain walls in the spin diagonal checkerboard state. If  $\delta = 1/8$  is assumed, the charge modulation pattern is consistent with the  $4a \times 4a$  charge structure observed in STM experiments.

We found that the coexistent state of bond-centered four-period diagonal and vertical spin-checkerboard structure characterized by a multi-Q set is stabilized and composed of  $4 \times 4$  period checkerboard spin

modulation.[151] In Fig.30(a), we show the condensation energies of some heterogeneous states,  $(E_{normal} - E_{hetero})/N_{site}$ , with fixing the transfer energies  $t' = -0.32$  and  $t'' = 0.22$  suitable for Bi-2212. The system is a  $16 \times 16$  lattice with the electron-filling  $\rho = N_e/N_{site} = 0.875$ . The energy of the normal state  $E_{normal}$  is calculated by adopting  $m_\ell = \rho_\ell = 0$ . In our calculations, the condensation energies of both bond-centered stripe and checkerboard states are always larger than those of site-centered stripe and checkerboard states. The vertical stripe state is not suitable in this parameter set since this state is only stabilized with the LSCO-type band. The four-period spin-diagonal checkerboard (DC) state is significantly more stable than the eight-period spin-DC state. We found that the coexistent state of the bond-centered four-period spin-DC and four-period spin-vertical checkerboard (VC) with  $\rho_\ell = 0$  is most stable, as shown in Fig.30(a). The measured expectation value of the spin density is shown in Fig.30(b).

### J. Improved Gutzwiller Function

We have presented the results based on the Gutzwiller functions for the normal state, SDW state and BCS state. We must consider a method to go beyond the Gutzwiller function-based Monte Carlo method. One method to achieve this purpose is to multiply the Jastrow correlation operators to take into account the intersite correlations. The simplest possible candidate is an introduction of the diagonal intersite correlation factor:[152]

$$\psi_{Jastrow} = \prod_{j\ell(\neq 0)} \prod_{\sigma\sigma'} [1 - (1 - g(\ell))n_{j\sigma}n_{j+\ell\sigma'}] \psi_n, \quad (54)$$

for the variational parameter  $g(\ell)$ . We have investigated the 2D Hubbard model by using the Jastrow-Gutzwiller function.[111] The ground-state energy is lowered considerably by considering the intersite correlations such as nearest neighbor and next nearest neighbor spin and charge correlations.

Here we consider the method to improve the wave functions by an off-diagonal Jastrow correlation operators.[94, 95, 153] The off-diagonal correlation factors are more effective to lower the ground state energy in 2D systems. Let us consider the wave functions  $\psi^{(m)}$  defined in the following way:[95]

$$\psi^{(1)} = \psi_G = e^{-\alpha V} \psi_0, \quad (55)$$

$$\psi^{(2)} = e^{-\lambda K} e^{-\alpha V} \psi_0, \quad (56)$$

$$\psi^{(3)} = e^{-\lambda' K} e^{-\alpha' V} \psi^{(2)}, \quad (57)$$

$$\dots \quad \dots \quad (58)$$

and so on, where  $K$  denotes the kinetic part of the Hamiltonian

$$K = -t \sum_{\langle ij \rangle \sigma} (c_{i\sigma}^\dagger c_{j\sigma} + \text{h.c.}), \quad (59)$$

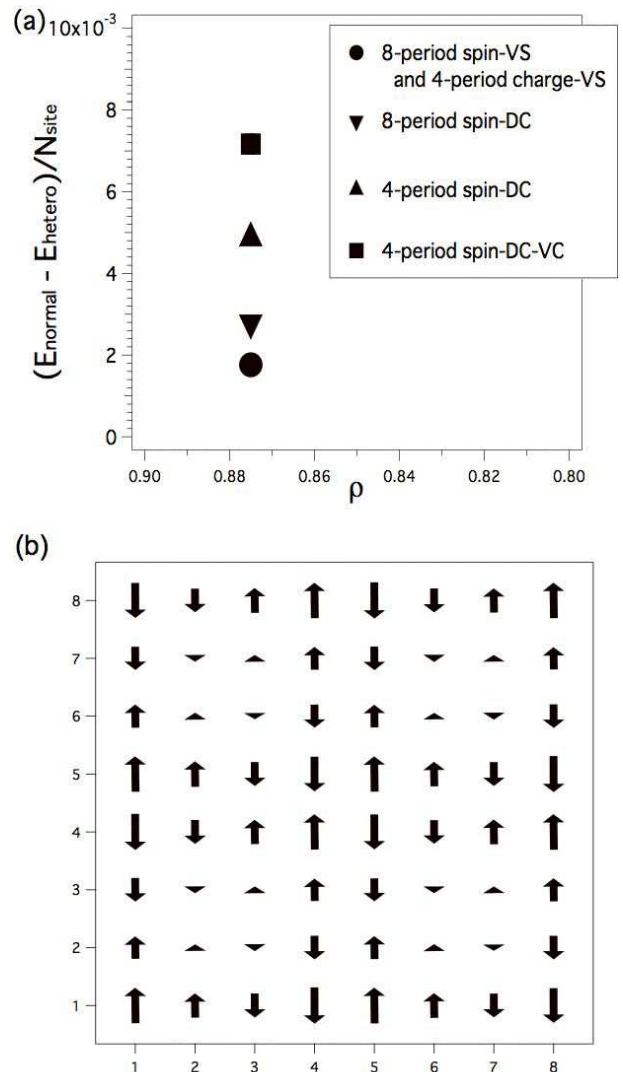


FIG. 30: (a) Condensation energies of inhomogeneous states with the bond-centered magnetic domain wall. The system is a  $16 \times 16$  lattice with  $t' = -0.32$ ,  $t'' = 0.22$ , and  $U = 8$  for the case of  $\rho = 0.875$ . The static error bars are smaller than the size of symbols. (b) Expectation value of the spin density  $m_i$  measured in the four-period spin-DC-VC solution. The length of arrows is proportional to the spin density.

and  $V$  denotes the on-site Coulomb interaction.  $\lambda$ ,  $\lambda'$ ,  $\lambda''$ ,  $\alpha$ ,  $\alpha'$  and  $\alpha''$  are variational parameters. It is considered that  $\psi^{(m)}$  approaches the true ground state wave function as  $m$  grows larger since the ground state wave function is written as

$$\psi = e^{-\beta H} \psi_0 \simeq e^{-\epsilon_1 K} e^{-\epsilon_1 V} \dots e^{-\epsilon_m K} e^{-\epsilon_m V} \psi_0, \quad (60)$$

for large  $\beta = \epsilon_1 + \dots + \epsilon_m$  and small  $\epsilon_i$  ( $i = 1, \dots, m$ ). If we can extrapolate the expectation values from the data for  $\psi^{(1)}$ ,  $\psi^{(2)}$ ,  $\dots$ , we can evaluate correct expectation values.

The computations are performed by using the discrete Hubbard-Stratonovich transformation as described

in Section III.A. In the evaluation of the expectation values we generate the Monte Carlo samples by the importance sampling[95] with the weight function  $|w| = |w_\uparrow w_\downarrow|$  where

$$w_\sigma = \det(\phi_0^{\sigma\dagger} \exp(V^\sigma(u, \alpha)) \cdots \exp(V^\sigma(s, \alpha) \phi_0^\sigma). \quad (61)$$

Since the Monte Carlo samplings are generated with the weight  $|w|$ , the expectation values are calculated with the sign of  $w$  in the summation over the generated samples. In our calculations the negative sign problem has become less serious due to the variational treatment, although we encounter the inevitable negative sign problem in the standard projector Monte Carlo approaches.[154]

In Fig.31 the energy is shown as a function of  $1/m$  where the SDW and normal states are chosen as the initial state  $\psi_0$ . The extrapolated values for different initial states coincide with each other within Monte Carlo statistical errors. The energy expectation values as a function of  $U$  for  $8 \times 8$  square lattice are presented in Fig.32 for  $\psi_n = \psi^{(1)}$ ,  $\psi_{AF}$ ,  $\psi^{(3)}$ . The extrapolated curve is shown by the solid curve and the results obtained by the quantum Monte Carlo simulation (QMC)[28] are also shown as a reference. A good agreement between two calculations support the method although the QMC gives slightly higher energy for  $U = 8$ .

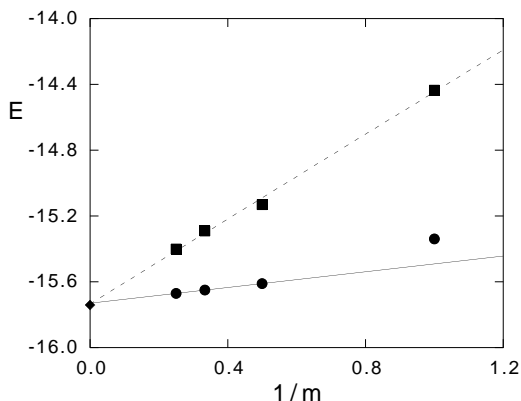


FIG. 31: Energy as a function of  $1/m$  for the single-band Hubbard model for  $N_e = 14$  and  $U = 4$  on the lattice of  $4 \times 4$  sites. For the upper and lower curves, the initial wave function  $\psi_0$  is the Fermi sea and SDW state, respectively. The diamond indicates the exact value obtained from the diagonalization.[95]

One can formulate an approach to consider the BCS function with correlation operators.[96] For this end the electron-hole transformation is introduced for the down spin[155]:  $d_{\mathbf{k}} = c_{-\mathbf{k}\downarrow}^\dagger$ ,  $d_{\mathbf{k}}^\dagger = c_{-\mathbf{k}\downarrow}$ . The up-spin electrons are unaltered.

We show the energy versus  $1/m$  in Fig.33 for  $\psi^{(m)}$  and  $\psi_s^{(m)}$ . From an extrapolation to the limit  $m \rightarrow \infty$ , both formulations predict the same limiting value for the energy. The energy is lowered considerably due to the correlation operators compared to that for the Gutzwiller function. The energy in the  $d$ -wave SC state is always lower than that in the normal state for each  $m$ . The

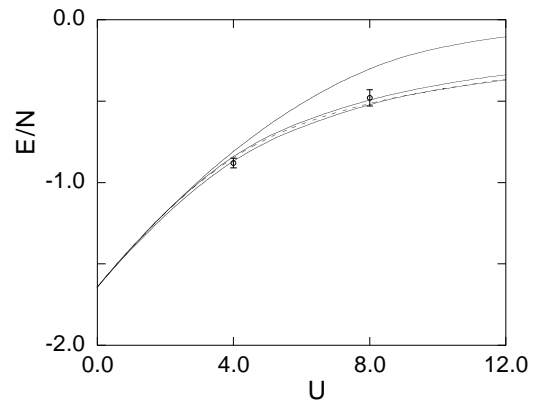


FIG. 32: Energy as a function of  $U$  for  $8 \times 8$  lattice at half-filling for the single-band Hubbard model. From the top the energies for  $\psi_n$ ,  $\psi_{AF}$ ,  $\psi^{(3)}$  and extrapolated values are shown. The quantum Monte Carlo results are shown by open circles.[95]

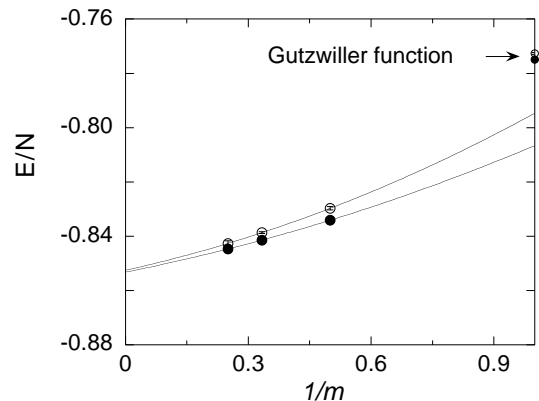


FIG. 33: The energy versus  $1/m$  for the single-band Hubbard model on the lattice of  $10 \times 10$  sites. Solid and open symbols are obtained for  $\psi_m$  with the normal and  $d$ -wave state initial functions  $\psi_0$  and  $\psi_{BCS}$ , respectively. Parameters are given by  $U = 8$ ,  $t' = -0.09$  and  $N_e = 80$ . [96]

energy gain in the SC state remains the same order after the multiplication of correlation factors.

### K. $T_c$ and $\epsilon_p - \epsilon_d$

Relationships between  $T_c$  and structural features in cuprate high-temperature superconductors are very interesting. Torrance and Metzger found the first such relationship between  $T_c$  and the Madelung potential difference  $\Delta V_M$ . [156] Here  $\Delta V_M$  is the potential difference between Cu and O sites in the  $\text{CuO}_2$  plane.  $T_c$  was found to increase with decreasing  $\Delta V_M$ . There is an interesting tendency of increasing  $T_c$  with increasing relative ratio of hole density at oxygen site against that at copper site.[117]

Here we show the results obtained by using the

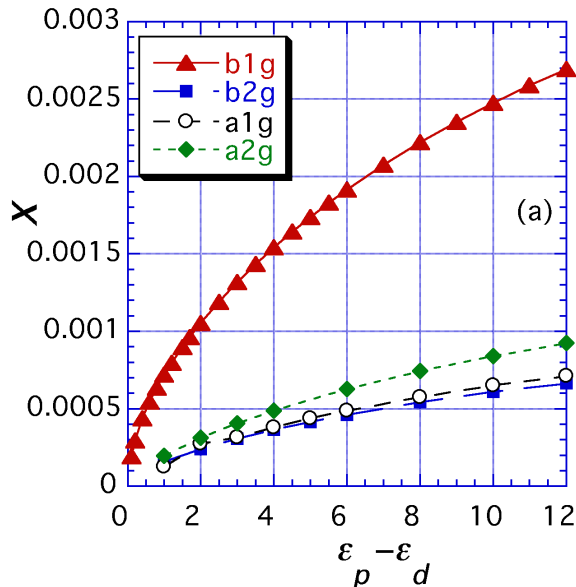


FIG. 34: The exponent  $x$  (superconductivity strength) as a function of  $\epsilon_p - \epsilon_d$ , where the level difference  $\epsilon_p - \epsilon_d$  is positive.

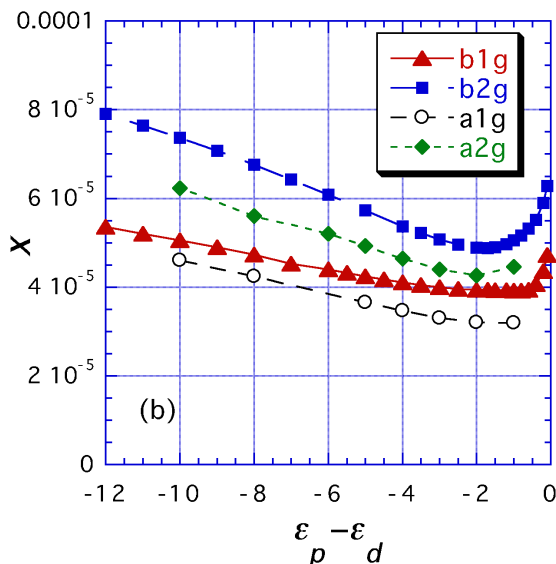


FIG. 35: The exponent  $x$  as a function of  $\epsilon_p - \epsilon_d$ , where the level difference  $\epsilon_p - \epsilon_d$  is negative.

perturbation theory[62–66]. There have been many similar works by making some kind of approximation such as Random phase approximation (RPA)[157–159], fluctuation-exchange approximation (FLEX)[160–163], effective spin-fluctuations[4, 164, 165], and perturbation theory in terms of  $U$ [166–168]. An application was made for  $\text{Sr}_2\text{RuO}_4$  where we need to consider the multi-band structure including  $\alpha$  and  $\beta$  orbitals[169], and also to the three-dimensional d-p model[170]. In our formulation the

gap function is written as

$$\Delta = \exp\left(-\frac{2}{xU_d^2}\right). \quad (62)$$

The exponent  $x$  indicates the strength of superconductivity. The results are in Figs. 34 and 35.[171] As shown in the figure, for positive  $\epsilon_p - \epsilon_d$ , with increase of  $\epsilon_p - \epsilon_d$  the exponent  $x$  increases monotonously. This means the increase of superconducting gap and so of  $T_c$ , and is consistent with the wide-range tendency of the variational Monte Carlo calculation.[24, 172] This tendency can be understood in terms of

$$U_{eff} = U_d \langle u_{\mathbf{k}}^0 \rangle^2 = \frac{U_d}{4} \left( 1 + \frac{1}{\sqrt{1 + 16t_{dp}^2/(\epsilon_p - \epsilon_d)^2}} \right)^2, \quad (63)$$

where  $u_{\mathbf{k}}^0$  is the weight of electrons. This clearly indicates that increase of  $\epsilon_p - \epsilon_d$  leads to the increase of  $U_{eff}$  and subsequently of  $x$ . In the case of  $\epsilon_p - \epsilon_d < 0$ , we take account of finite Coulomb repulsion  $U_p$  on oxygen sites. The effective interaction coming from  $U_p$  is similarly given by the susceptibility with the weight of  $p$  electrons. The results of  $x$  with  $U_p/U_d = 6/8$  indicates that all four types of even parity ( $b_{1g}$ ,  $b_{2g}$ ,  $a_{1g}$  and  $a_{2g}$ ) SC strength values increase, so that  $T_c$  is raised, as the absolute value  $|\epsilon_p - \epsilon_d|$  increases in this region. This result shows that  $U_p$  also plays an important role as well.

Let us give a discussion on this result. Increase of  $|\epsilon_p - \epsilon_d|$  in the region of  $\epsilon_p - \epsilon_d < 0$  means decrease of  $\Delta V_M = |e|(V_M^O - V_M^{Cu})$  since  $\epsilon_p - \epsilon_d = (A_2^O - I_3^{Cu}) + |e|(V_M^O - V_M^{Cu})$ , where  $A_2^O$  is the second electron affinity of oxygen atom and  $I_3^{Cu}$  is the third electron ionicity of copper atom and  $e$  is the charge of electron. Therefore, this relation is consistent with the systematics reported in [156]. With increase of the distance of the apex oxygen away from the  $\text{CuO}_2$  plane, cuprate superconductors are known to increase  $T_c$ . [173] The accompanying raise of  $\epsilon_d$  should tend to increase  $T_c$ .

The Coulomb interaction between  $p$  electrons on oxygen atom will raise the level of  $p$  electrons effectively. This leads to the lowering of  $p$  hole level  $\epsilon_p$  or the raise of  $\epsilon_d$  relatively. This indicates that  $T_c$  will be increased by the Coulomb interaction between  $p$  electrons.

## IV. QUANTUM MONTE CARLO STUDIES

### A. Quantum Monte Carlo Method

The Quantum Monte Carlo (QMC) method is a numerical method that is employed to simulate the behavior of correlated electron systems. We outline the QMC method in this section. The Hamiltonian is the Hubbard model that contains the on-site Coulomb repulsion and is written as

$$H = - \sum_{ij\sigma} t_{ij} (c_{i\sigma}^\dagger c_{j\sigma} + h.c.) + U \sum_j n_{j\uparrow} n_{j\downarrow}, \quad (64)$$

where  $c_{j\sigma}^\dagger$  ( $c_{j\sigma}$ ) is the creation (annihilation) operator of an electron with spin  $\sigma$  at the  $j$ -th site and  $n_{j\sigma} = c_{j\sigma}^\dagger c_{j\sigma}$ .  $t_{ij}$  is the transfer energy between the sites  $i$  and  $j$ .  $t_{ij} = t$  for the nearest-neighbor bonds. For all other cases  $t_{ij} = 0$ .  $U$  is the on-site Coulomb energy. The number of sites is  $N$  and the linear dimension of the system is denoted as  $L$ . The energy unit is given by  $t$  and the number of electrons is denoted as  $N_e$ .

In a Quantum Monte Carlo simulation, the ground state wave function is

$$\psi = e^{-\tau H} \psi_0, \quad (65)$$

where  $\psi_0$  is the initial one-particle state represented by a Slater determinant. For large  $\tau$ ,  $e^{-\tau H}$  will project out the ground state from  $\psi_0$ . We write the Hamiltonian as  $H = K + V$  where  $K$  and  $V$  are the kinetic and interaction terms of the Hamiltonian in Eq.(64), respectively. The wave function in Eq.(65) is written as

$$\psi = (e^{-\Delta\tau(K+V)})^M \psi_0 \approx (e^{-\Delta\tau K} e^{-\Delta\tau V})^M \psi_0, \quad (66)$$

for  $\tau = \Delta\tau \cdot M$ . Using the Hubbard-Stratonovich transformation[27, 94], we have

$$\begin{aligned} \exp(-\Delta\tau U n_{i\uparrow} n_{i\downarrow}) &= \frac{1}{2} \sum_{s_i = \pm 1} \exp(2as_i(n_{i\uparrow} - n_{i\downarrow}) \\ &\quad - \frac{1}{2} U \Delta\tau (n_{i\uparrow} + n_{i\downarrow})), \end{aligned} \quad (67)$$

for  $(\tanh a)^2 = \tanh(\Delta\tau U/4)$  or  $\cosh(2a) = e^{\Delta\tau U/2}$ . The wave function is expressed as a summation of the one-particle Slater determinants over all the configurations of the auxiliary fields  $s_j = \pm 1$ . The exponential operator is expressed as

$$\begin{aligned} (e^{-\Delta\tau K} e^{-\Delta\tau V})^M &= \frac{1}{2^{NM}} \sum_{\{s_i(\ell)\}} \prod_{\sigma} B_M^{\sigma}(s_i(M)) \\ &\quad \times B_{M-1}^{\sigma}(s_i(M-1)) \cdots B_1^{\sigma}(s_i(1)), \end{aligned} \quad (68)$$

where we have defined

$$B_{\ell}^{\sigma}(\{s_i(\ell)\}) = e^{-\Delta\tau K_{\sigma}} e^{-V_{\sigma}(\{s_i(\ell)\})}, \quad (69)$$

for

$$V_{\sigma}(\{s_i\}) = 2a\sigma \sum_i s_i n_{i\sigma} - \frac{1}{2} U \Delta\tau \sum_i n_{i\sigma}, \quad (70)$$

$$K_{\sigma} = - \sum_{ij} t_{ij} (c_{i\sigma}^\dagger c_{j\sigma} + h.c.). \quad (71)$$

The ground-state wave function is

$$\psi = \sum_m c_m \phi_m, \quad (72)$$

where  $\phi_m$  is a Slater determinant corresponding to a configuration  $m = \{s_i(\ell)\}$  ( $i = 1, \dots, N; \ell = 1, \dots, M$ ) of the auxiliary fields:

$$\begin{aligned} \phi_m &= \prod_{\sigma} B_M^{\sigma}(s_i(M)) \cdots B_1^{\sigma}(s_i(1)) \psi_0 \\ &\equiv \phi_m^{\uparrow} \phi_m^{\downarrow}. \end{aligned} \quad (73)$$

The coefficients  $c_m$  are constant real numbers:  $c_1 = c_2 = \dots$ . The initial state  $\psi_0$  is a one-particle state. If electrons occupy the wave numbers  $k_1, k_2, \dots, k_{N_{\sigma}}$  for each spin  $\sigma$ ,  $\psi_0$  is given by the product  $\psi_0^{\uparrow} \psi_0^{\downarrow}$  where  $\psi_0^{\sigma}$  is the matrix represented as[31]

$$\begin{pmatrix} e^{ik_1 \cdot r_1} & e^{ik_2 \cdot r_1} & \dots & \dots & e^{ik_{N_{\sigma}} \cdot r_1} \\ e^{ik_1 \cdot r_2} & e^{ik_2 \cdot r_2} & \dots & \dots & \dots \\ \cdot & \cdot & \cdot & \cdot & \cdot \\ e^{ik_1 \cdot r_N} & e^{ik_2 \cdot r_N} & \dots & \dots & \dots \end{pmatrix}. \quad (74)$$

$N_{\sigma}$  is the number of electrons for spin  $\sigma$ . In actual calculations we can use a real representation where the matrix elements are  $\cos(k_i \cdot r_j)$  or  $\sin(k_i \cdot r_j)$ . In the real-space representation, the matrix of  $V_{\sigma}(\{s_i\})$  is a diagonal matrix given as

$$V_{\sigma}(\{s_i\}) = \text{diag}(2a\sigma s_1 - U\Delta\tau/2, \dots, 2a\sigma s_N - U\Delta\tau/2). \quad (75)$$

The matrix elements of  $K_{\sigma}$  are

$$\begin{aligned} (K_{\sigma})_{ij} &= -t \quad i, j \text{ are nearest neighbors} \\ &= 0 \quad \text{otherwise.} \end{aligned} \quad (76)$$

$\phi_m^{\sigma}$  is an  $N \times N_{\sigma}$  matrix given by the product of the matrices  $e^{-\Delta\tau K_{\sigma}}$ ,  $e^{V_{\sigma}}$  and  $\psi_0^{\sigma}$ . The inner product is thereby calculated as a determinant[38],

$$\langle \phi_m^{\sigma} \phi_n^{\sigma} \rangle = \det(\phi_m^{\sigma \dagger} \phi_n^{\sigma}). \quad (77)$$

The expectation value of the quantity  $Q$  is evaluated as

$$\langle Q \rangle = \frac{\sum_{mn} \langle \phi_m Q \phi_n \rangle}{\sum_{mn} \langle \phi_m \phi_n \rangle}. \quad (78)$$

If  $Q$  is a bilinear operator  $Q_{\sigma}$  for spin  $\sigma$ , we have

$$\begin{aligned} \langle Q_{\sigma} \rangle &= \frac{\sum_{mn} \langle \phi_m^{\sigma} Q_{\sigma} \phi_n^{\sigma} \rangle \langle \phi_m^{-\sigma} \phi_n^{-\sigma} \rangle}{\sum_{mn} \langle \phi_m^{\sigma} \phi_n^{\sigma} \rangle \langle \phi_m^{-\sigma} \phi_n^{-\sigma} \rangle} \\ &= \frac{\sum_{mn} \langle \phi_m^{\sigma} Q_{\sigma} \phi_n^{\sigma} \rangle \det(\phi_m^{-\sigma \dagger} \phi_n^{-\sigma})}{\sum_{mn} \det(\phi_m^{\sigma \dagger} \phi_n^{\sigma}) \det(\phi_m^{-\sigma \dagger} \phi_n^{-\sigma})} \\ &= \sum_{mn} \frac{\det(\phi_m^{\sigma \dagger} \phi_n^{\sigma}) \det(\phi_m^{-\sigma \dagger} \phi_n^{-\sigma})}{\sum_{m'n'} \det(\phi_m^{\sigma \dagger} \phi_n^{\sigma}) \det(\phi_m'^{-\sigma \dagger} \phi_n'^{-\sigma})} \\ &\quad \times \frac{\langle \phi_m^{\sigma} Q_{\sigma} \phi_n^{\sigma} \rangle}{\langle \phi_m^{\sigma} \phi_n^{\sigma} \rangle}. \end{aligned} \quad (79)$$

The expectation value with respect to the Slater determinants  $\langle \phi_m^{\sigma} Q_{\sigma} \phi_n^{\sigma} \rangle$  is evaluated using the single-particle Green's function[31, 38],

$$\frac{\langle \phi_m^{\sigma} c_{i\sigma} c_{j\sigma}^{\dagger} \phi_n^{\sigma} \rangle}{\langle \phi_m^{\sigma} \phi_n^{\sigma} \rangle} = \delta_{ij} - (\phi_n^{\sigma} (\phi_m^{\sigma \dagger} \phi_n^{\sigma})^{-1} \phi_m^{\sigma \dagger})_{ij}. \quad (80)$$

In the above expression,

$$P_{mn} \equiv \det(\phi_m^\sigma \phi_n^\sigma) \det(\phi_m^{-\sigma} \phi_n^{-\sigma}) \quad (81)$$

can be regarded as the weighting factor to obtain the Monte Carlo samples. Since this quantity is not necessarily positive definite, the weighting factor should be  $|P_{mn}|$ ; the resulting relationship is,

$$\begin{aligned} \langle Q_\sigma \rangle &= \frac{\sum_{mn} P_{mn} \langle Q_\sigma \rangle_{mn}}{\sum_{mn} P_{mn}} \\ &= \frac{\sum_{mn} |P_{mn}| \text{sign}(P_{mn}) \langle Q_\sigma \rangle_{mn}}{\sum_{mn} |P_{mn}| \text{sign}(P_{mn})} \end{aligned} \quad (82)$$

where  $\text{sign}(a) = a/|a|$  and

$$\langle Q_\sigma \rangle_{mn} = \frac{\langle \phi_m^\sigma Q_\sigma \phi_n^\sigma \rangle}{\langle \phi_m^\sigma \phi_n^\sigma \rangle}. \quad (83)$$

This relation can be evaluated using a Monte Carlo procedure if an appropriate algorithm, such as the Metropolis or heat bath method, is employed[94]. The summation can be evaluated using appropriately defined Monte Carlo samples,

$$\langle Q_\sigma \rangle = \frac{\frac{1}{n_{MC}} \sum_{mn} \text{sign}(P_{mn}) \langle Q_\sigma \rangle_{mn}}{\frac{1}{n_{MC}} \sum_{mn} \text{sign}(P_{mn})}, \quad (84)$$

where  $n_{MC}$  is the number of samples. The sign problem is an issue if the summation of  $\text{sign}(P_{mn})$  vanishes within statistical errors. In this case it is indeed impossible to obtain definite expectation values.

## B. Quantum Monte Carlo Diagonalization

### 1. Basic Method and Optimization

Quantum Monte Carlo diagonalization (QMD) is a method for the evaluation of  $\langle Q_\sigma \rangle$  without the *negative sign problem*. [41] A bosonic version of this method was developed before in Ref.[174]. The configuration space of the probability  $\|P_{mn}\|$  in Eq.(84) is generally very strongly peaked. The sign problem lies in the distribution of  $P_{mn}$  in the configuration space. It is important to note that the distribution of the basis functions  $\phi_m$  ( $m = 1, 2, \dots$ ) is uniform since  $c_m$  are constant numbers:  $c_1 = c_2 = \dots$ . In the subspace  $\{\phi_m\}$ , selected from all configurations of auxiliary fields, the right-hand side of Eq.(78) can be determined. However, the large number of basis states required to obtain accurate expectation values is beyond the current storage capacity of computers. Thus we use the variational principle to obtain the expectation values.

From the variational principle,

$$\langle Q \rangle = \frac{\sum_{mn} c_m c_n \langle \phi_m Q \phi_n \rangle}{\sum_{mn} c_m c_n \langle \phi_m \phi_n \rangle}, \quad (85)$$

where  $c_m$  ( $m = 1, 2, \dots$ ) are variational parameters. In order to minimize the energy

$$E = \frac{\sum_{mn} c_m c_n \langle \phi_m H \phi_n \rangle}{\sum_{mn} c_m c_n \langle \phi_m \phi_n \rangle}, \quad (86)$$

the equation  $\partial E / \partial c_n = 0$  ( $n = 1, 2, \dots$ ) is solved for,

$$\sum_m c_m \langle \phi_n H \phi_m \rangle - E \sum_m c_m \langle \phi_n \phi_m \rangle = 0. \quad (87)$$

If we set

$$H_{mn} = \langle \phi_m H \phi_n \rangle, \quad (88)$$

$$A_{mn} = \langle \phi_m \phi_n \rangle, \quad (89)$$

the eigen-equation is

$$Hu = EAu, \quad (90)$$

for  $u = (c_1, c_2, \dots)^t$ . Since  $\phi_m$  ( $m = 1, 2, \dots$ ) are not necessarily orthogonal,  $A$  is not a diagonal matrix. We diagonalize the Hamiltonian  $A^{-1}H$ , and then calculate the expectation values of correlation functions with the ground state eigenvector.

In Quantum Monte Carlo simulations an extrapolation is performed to obtain the expectation values for the ground-state wave function. If  $M$  is large enough, the wave function in Eq.(72) will approach the exact ground-state wave function,  $\psi_{exact}$ , as the number of basis functions,  $N_{states}$ , is increased. If the number of basis functions is large enough, the wave function will approach,  $\psi_{exact}$ , as  $M$  is increased. In either case the method employed for the reliable extrapolation of the wave function is a key issue in calculating the expectation values. The variance method was recently proposed in variational and Quantum Monte Carlo simulations, where the extrapolation is performed as a function of the energy variance. We can expect linearity in some cases[175]:

$$\langle Q \rangle - Q_{exact} \propto v, \quad (91)$$

where  $v$  denotes the variance defined as

$$v = \frac{\langle (H - \langle H \rangle)^2 \rangle}{\langle H \rangle^2} \quad (92)$$

and  $Q_{exact}$  is the expected exact value of the quantity  $Q$ .

The simplest procedure for optimizing the ground-state wave function is to increase the number of basis states  $\{\phi_m\}$  by random sampling. First, we set  $\tau$  and  $M$ , for example,  $\tau = 0.1, 0.2, \dots$ , and  $M = 20, 30, \dots$ . We denote the number of basis functions as  $N_{states}$ . We start with  $N_{states} = 100 \sim 300$  and then increase up to 10000. This procedure can be outlined as follows:

A1. Generate the auxiliary fields  $s_i$  ( $i = 1, \dots, N$ ) in  $B_\ell^\sigma(\{s_i\})$  randomly for  $\ell = 1, \dots, M$  for  $\phi_m$  ( $m = 1, \dots, N_{states}$ ), and generate  $N_{states}$  basis wave function  $\{\phi_m\}$ .

A2. Evaluate the matrices  $H_{mn} = \langle \phi_m | H | \phi_n \rangle$  and  $A_{mn} = \langle \phi_m | \phi_n \rangle$ , and diagonalize the matrix  $A^{-1}H$  to obtain  $\psi = \sum_m c_m \phi_m$ . Then calculate the expectation values and the energy variance.

A3. Repeat the procedure from A1 after increasing the number of basis functions.

For small systems this random method produces reliable energy results. The diagonalization plays an importance producing fast convergence. In order to lower the ground-state energy efficiently, we can employ a genetic algorithm[176] to generate the basis set from the initial basis set. One idea is to replace some parts of  $\{s_i(\ell)\}$  ( $i = 1, \dots, N; \ell = 1, \dots, M$ ) in  $\phi_n$  that has the large weight  $|c_n|^2$  to generate a new basis function  $\phi'_n$ . The new basis function  $\phi'_n$  obtained in this way is expected to also have a large weight and contribute to  $\psi$ . The details of the method are shown in Ref.[41].

## 2. Ground State Energy and Correlation Functions

The energy as a function of the variance is presented in Figs.36, 37 and 38 for  $4 \times 4$ ,  $6 \times 2$  and  $6 \times 6$ , respectively. To obtain these results the genetic algorithm was employed to produce the basis functions except the open symbols in Fig.37. The  $4 \times 4$  where  $N_e = 10$  in Fig.36 is the energy for the closed shell case up to 2000 basis states. The other two figures are for open shell cases, where evaluations were performed up to 3000 states. We show the results for the  $4 \times 4$ ,  $6 \times 2$  and  $6 \times 6$  systems in Table II.

The Fig. 39 is the momentum distribution function  $n(\mathbf{k})$ ,

$$n(\mathbf{k}) = \frac{1}{2} \sum_{\sigma} \langle c_{\mathbf{k}\sigma}^{\dagger} c_{\mathbf{k}\sigma} \rangle, \quad (93)$$

for  $14 \times 14$  sites where the results for the Gutzwiller VMC and the QMD are indicated. The Gutzwiller function gives the results that  $n(k)$  increases as  $k$  approaches  $k_F$  from above the Fermi surface. This is clearly unphysical. This flaw of the Gutzwiller function near the Fermi surface is not observed for the QMD result.

## 3. Spin Gap in the Hubbard Ladder

Here we show the results for one-dimensional models. The ground state of the 1D Hubbard model is no longer Fermi liquid for  $U > 0$ . The ground state is insulating at half-filling and metallic for less than half-filling. The Fig. 40 is the spin and charge correlation functions,  $S(k)$  and  $C(k)$ , as a function of the wave number, for the 1D Hubbard model where  $N = 80$ . The  $2k_F$  singularity can be clearly identified where the dotted line is for  $U = 0$ . The

TABLE II: Ground state energy per site from the Hubbard model. The boundary conditions are periodic in both directions. The current results are presented under the column labeled QMD. The constrained path Monte Carlo (CPMC) results are from Refs.[38]. The column VMC is the results obtained for the optimized variational wave function  $\psi_{\lambda}^{(2)}$  except for  $6 \times 2$  for which  $\psi_{\lambda}^{(1)}$  is employed. The QMC results are from Ref.[35]. Exact results are obtained using diagonalization[177].

Size	$N_e$	$U$	QMD	VMC	CPMC	QMC	Exact
$4 \times 4$	10	4	-1.2237	-1.221(1)	-1.2238		-1.2238
$4 \times 4$	14	4	-0.9836	-0.977(1)	-0.9831		-0.9840
$4 \times 4$	14	8	-0.732(2)	-0.727(1)	-0.7281		-0.7418
$4 \times 4$	14	10	-0.656(2)	-0.650(1)			-0.6754
$4 \times 4$	14	12	-0.610(4)	-0.607(2)	-0.606		-0.6282
$6 \times 2$	10	2	-1.058(1)	-1.040(1)			-1.05807
$6 \times 2$	10	4	-0.873(1)	-0.846(1)			-0.8767
$6 \times 6$	34	4	-0.921(1)	-0.910(2)		-0.925	
$6 \times 6$	36	4	-0.859(2)	-0.844(2)		-0.8608	

spin correlation is enhanced and the charge correlation function is suppressed slightly because of the Coulomb interaction.

The spin correlation function  $S(\mathbf{k})$  for the Hubbard ladder is presented in Fig.41, where  $U = 4$  and  $t_d = 1$ .  $S(\mathbf{k})$  is defined as

$$S(\mathbf{k}) = \frac{1}{N} \sum_{i\ell, j\ell'} e^{i\mathbf{k} \cdot (\mathbf{R}_{i\ell} - \mathbf{R}_{j\ell'})} \langle (n_{\ell i \uparrow} - n_{\ell i \downarrow})(n_{\ell' j \uparrow} - n_{\ell' j \downarrow}) \rangle, \quad (94)$$

where  $\mathbf{R}_{i\ell}$  denotes the site  $(i, \ell)$  ( $\ell=1,2$ ). We use the convention that  $\mathbf{k} = (k, k_y)$  where  $k_y = 0$  and  $\pi$  indicate the lower band and upper band, respectively. There are four singularities at  $2k_{F1}$ ,  $2k_{F2}$ ,  $k_{F1} - k_{F2}$ , and  $k_{F1} + k_{F2}$  for the Hubbard ladder, where  $k_{F1}$  and  $k_{F2}$  are the Fermi wave numbers of the lower and upper band, respectively.

It has been expected that the charge gap opens up as  $U$  turns on at half-filling for the Hubbard ladder model. In Fig.42 the charge gap at half-filling is shown as a function of  $U$ . The charge gap is defined as

$$\Delta_c = E(N_e + 2) + E(N_e - 2) - 2E(N_e), \quad (95)$$

where  $E(N_e)$  is the ground state energy for the  $N_e$  electrons. The charge gap in Fig.42 was estimated using the extrapolation to the infinite system from the data for the  $20 \times 2$ ,  $30 \times 2$ , and  $40 \times 2$  systems. The data suggest the exponentially small charge gap for small  $U$  or the existence of the critical value  $U_c$  in the range of  $0 \leq U_c < 1.5$ , below which the charge gap vanishes.

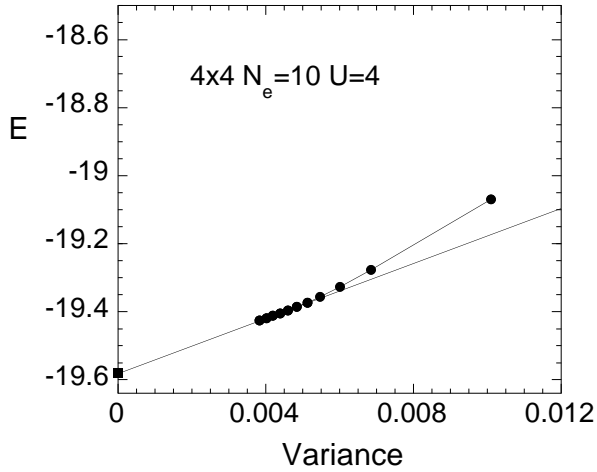


FIG. 36: Energy as a function of the variance for  $4 \times 4$ ,  $U = 4$  and  $N_e = 10$ . The square is the exact result. The data fit using a straight line using the least-square method as the variance is reduced. We started with  $N_{states} = 100$  (first solid circle) and then increase up to 2000.

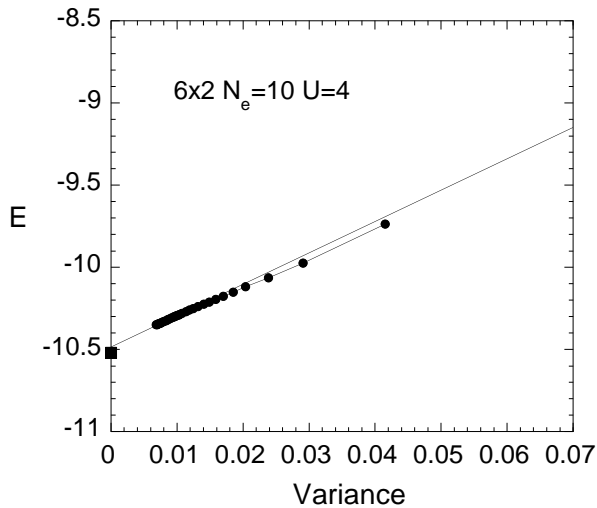


FIG. 37: Energy as a function of the variance for  $6 \times 2$   $N_e = 10$  and  $U = 4$ . The square is the exact value obtained using exact diagonalization.

#### 4. Magnetization in 2D Hubbard Model

The ground state of the 2D Hubbard model at half-filling is antiferromagnetic for  $U > 0$  because of the nesting due to the commensurate vector  $Q = (\pi, \pi)$ . The Gutzwiller function predicts that the magnetization

$$m = \left| \frac{1}{N} \sum_j (n_{j\uparrow} - n_{j\downarrow}) e^{iQ \cdot R_j} \right| \quad (96)$$

increases rapidly as  $U$  increases and approaches  $m = 1$  for large  $U$ . In Fig.43 the QMD results are presented for  $m$  as a function of  $U$ . The previous results obtained using

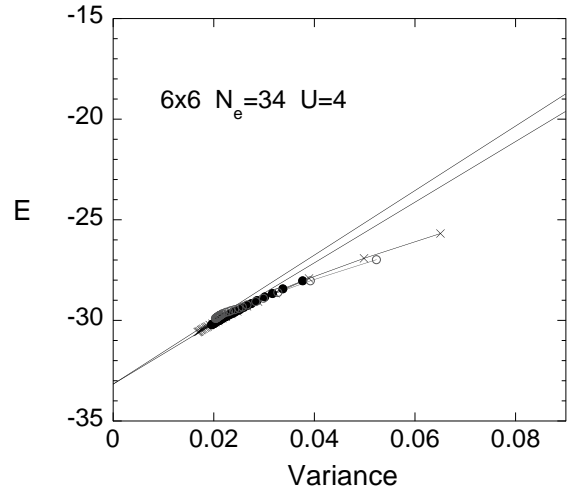


FIG. 38: Energy as a function of the variance  $v$  for  $6 \times 6$ . with the periodic boundary conditions. Solid circles and crosses are data obtained from the QMD method for two different initial configurations of the auxiliary fields. Gray open circles show results obtained from a simple  $1/2^N$ -method with 300 basis wave functions[41].

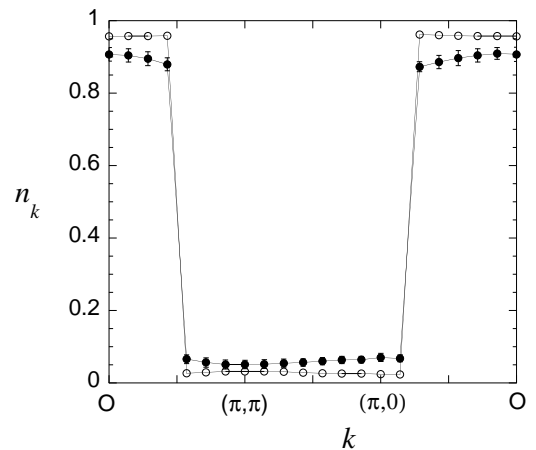


FIG. 39: Momentum distribution function for the  $14 \times 14$  lattice. Parameters are  $U = 4$  and  $N_e = 146$ . The boundary conditions are periodic in both directions. The results for the Gutzwiller function (open circle) are also provided.

the QMC method are plotted as open circles. The gray circles are for the  $\lambda$ -function VMC method and squares are the Gutzwiller VMC data. Clearly, the magnetization is reduced considerably because of the fluctuations, and is smaller than the Gutzwiller VMC method by about 50 percent.

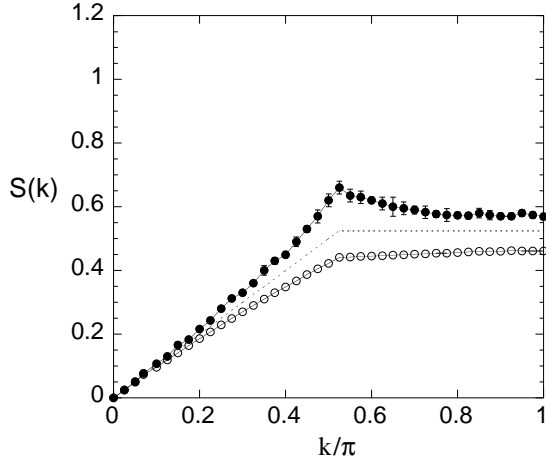


FIG. 40: Spin (solid circle) and charge (open circle) correlation functions obtained from the QMD method for the one-dimensional Hubbard model with 80 sites. The number of electrons is 66. We set  $U = 4$  and use the periodic boundary condition.

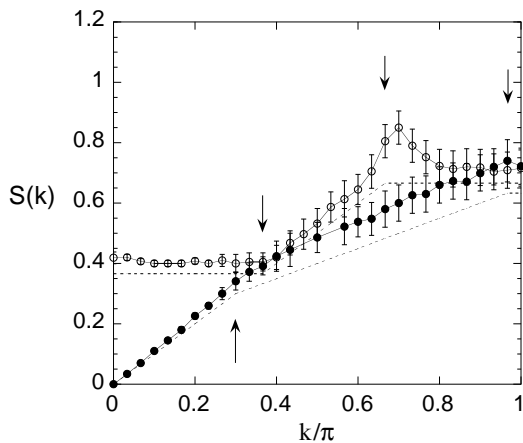


FIG. 41: Spin correlation function obtained from the QMD method for the ladder Hubbard model for  $60 \times 2$  sites with periodic boundary condition. The number of electrons is 80 and  $U = 4$ . The upper line is for the upper band and the lower line is for the lower band. Singularities are at  $k_{F1} - k_{F2}$ ,  $2k_{F2}$ ,  $k_{F1} + k_{F2}$  and  $2k_{F1}$  from left. The dotted lines are for  $U = 0$ .

### C. Pair Correlation Function

The pair correlation function  $D_{\alpha\beta}$  is defined by

$$D_{\alpha\beta}(\ell) = \langle \Delta_{\alpha}^{\dagger}(i + \ell) \Delta_{\beta}(i) \rangle, \quad (97)$$

where  $\Delta_{\alpha}(i)$ ,  $\alpha = x, y$ , denote the annihilation operators of the singlet electron pairs for the nearest-neighbor sites:

$$\Delta_{\alpha}(i) = c_{i\downarrow} c_{i+\hat{\alpha}\uparrow} - c_{i\uparrow} c_{i+\hat{\alpha}\downarrow}. \quad (98)$$

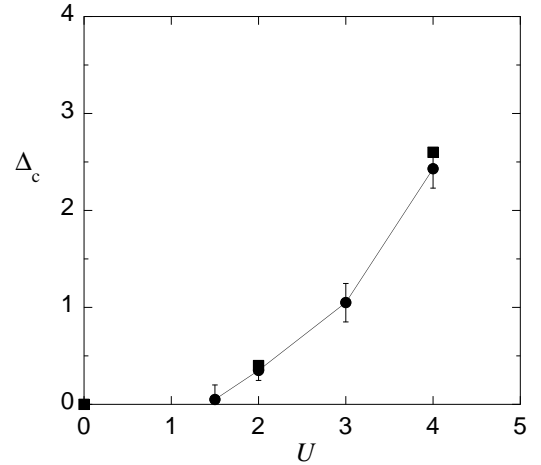


FIG. 42: Charge gap as a function of  $U$  for  $t_d = 1$  (circles). The DMRG results (squares) are provided for comparison[58].

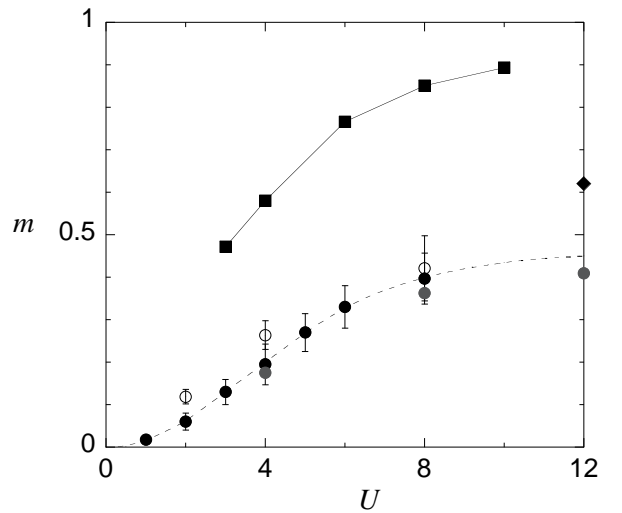


FIG. 43: Magnetization as a function of  $U$  for the half-filled Hubbard model after extrapolation at the limit of large  $N$ . Solid circles are the QMD results, and open circles are results obtained from the QMC method[28]. The squares are the Gutzwiller-VMC results[43] and gray solid circles show the 3rd  $\lambda$ -function ( $\psi_{\lambda}^{(3)}$ ) VMC results carried out on the  $8 \times 8$  lattice[95]. The diamond symbol is the value from the two-dimensional Heisenberg model where  $m = 0.615$ [179, 180].

Here  $\hat{\alpha}$  is a unit vector in the  $\alpha (= x, y)$ -direction. We consider the correlation function of d-wave pairing:

$$P_d(\ell) = \langle \Delta_d(i + \ell)^{\dagger} \Delta_d(i) \rangle, \quad (99)$$

where

$$\Delta_d(i) = \Delta_x(i) + \Delta_{-x}(i) - \Delta_y(i) - \Delta_{-y}(i). \quad (100)$$

$i$  and  $i + \ell$  denote sites on the lattice.

We show how the pair correlation function is evaluated in quantum Monte Carlo methods. We show the pair correlation functions  $D_{yy}$  and  $D_{yx}$  on the lattice

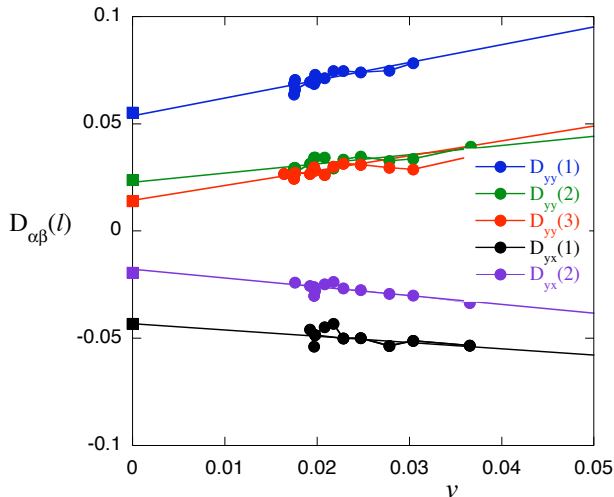


FIG. 44: Pair correlation function  $D_{yy}(\ell)$  and  $D_{yx}(\ell)$  for  $4 \times 3$ ,  $U = 4$  and  $N_e = 10$  obtained by the diagonalization quantum Monte Carlo method. The square are the exact results obtained by the exact diagonalization method. The data fit using a straight line using the least-square method as the variance is reduced. We started with  $N_{states} = 100$  (first solid circles) and then increase up to 2000.

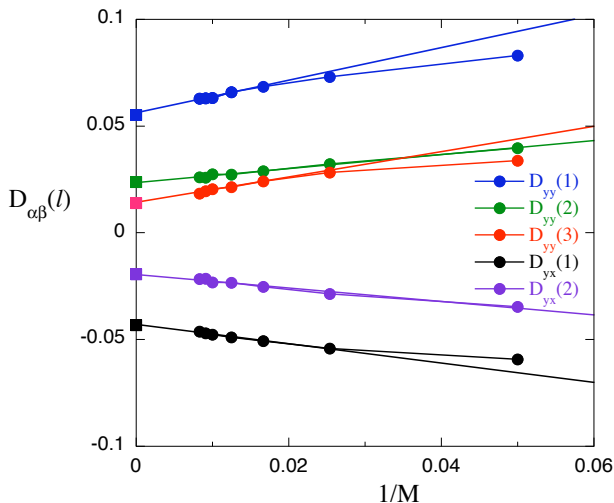


FIG. 45: Pair correlation function  $D_{yy}(\ell)$  and  $D_{yx}(\ell)$  for  $4 \times 3$ ,  $U = 4$  and  $N_e = 10$  obtained by the Metropolis quantum Monte Carlo method. The square are the exact results obtained by the exact diagonalization method. An extrapolation is performed as a function of  $1/M$ .

$4 \times 3$  in Figs.44 and 45. The boundary condition is open in the 4-site direction and is periodic in the other direction. An extrapolation is performed as a function of  $1/M$  in the QMC method with Metropolis algorithm and as a function of the energy variance  $v$  in the QMD method with diagonalization. We keep  $\Delta\tau$  a small constant  $\simeq 0.02 \sim 0.05$  and increase  $\tau = \Delta\tau \cdot M$ , where  $M$  is the division number. In the Metropolis QMC method, we calculated averages over  $5 \times 10^5$  Monte Carlo steps. The exact values were obtained by using the exact

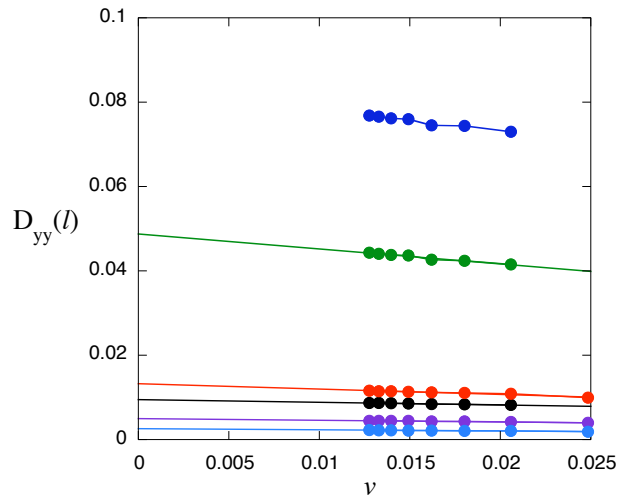


FIG. 46: Pair correlation function  $D_{yy}(\ell)$  as a function of the energy variance  $v$  for  $30 \times 2$ ,  $U = 4$  and  $N_e = 48$  obtained by the diagonalization quantum Monte Carlo method.

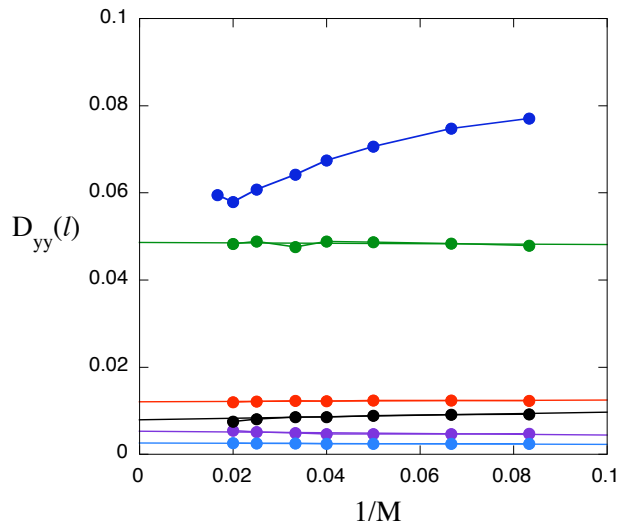


FIG. 47: Pair correlation function  $D_{yy}(\ell)$  as a function of  $1/M$  for  $30 \times 2$ ,  $U = 4$  and  $N_e = 48$  obtained by the Metropolis quantum Monte Carlo method.

diagonalization method. Two methods give consistent results as shown in figures. All the  $D_{yy}(\ell)$  and  $D_{yx}(\ell)$  are suppressed on  $4 \times 3$  as  $U$  is increased. In general, the pair correlation functions are suppressed in small systems. In Figs.46 and 47, we show the inter-chain pair correlation function for the ladder model  $30 \times 2$ . We use the open boundary condition. The number of electrons is  $N_e = 48$ , and the strength of the Coulomb interaction is  $U = 4$ .  $\Delta_y(i)$  indicates the electron pair along the rung, and  $D_{yy}(\ell)$  is the expectation value of the parallel movement of the pair along the ladder. The results obtained by two methods are in good agreement except  $\ell = (1, 0)$  (nearest-neighbor correlation).

We first consider the half-filled case with  $t' = 0$ ; in this case the antiferromagnetic correlation is dominant

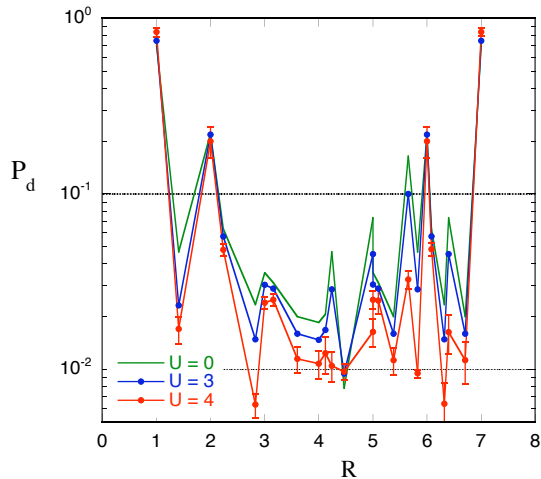


FIG. 48: Pair correlation function  $P_d$  as a function of the distance  $R = |\ell|$  on  $8 \times 8$  lattice for the half-filled case  $N_e = 64$ . We set  $t' = 0.0$  and  $U = 0, 3$  and  $4$ . To lift the degeneracy of electron configurations at the Fermi energy in the half-filled case, we included a small staggered magnetization  $\sim 10^{-4}$  in the initial wave function  $\psi_0$ .

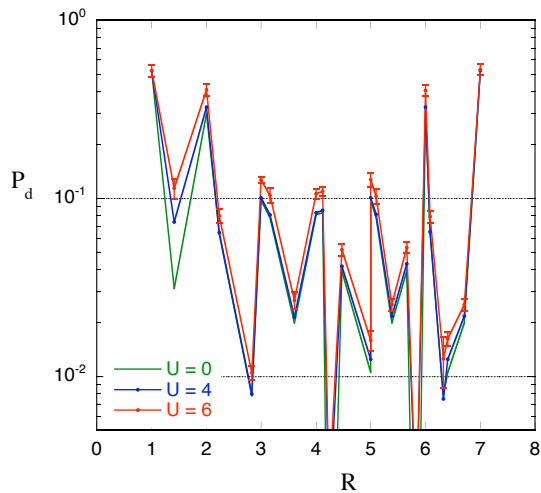


FIG. 49: Pair correlation function  $P_d$  as a function of the distance  $R = |\ell|$  on  $8 \times 8$  lattice for  $N_e = 54$ . We set  $t' = -0.2$  and  $U = 0, 4$  and  $6$ .

over the superconductive pairing correlation and thus the pairing correlation function is suppressed as the Coulomb repulsion  $U$  is increased. The Fig.48 exhibits the d-wave pairing correlation function  $P_d$  on  $8 \times 8$  lattice as a function of the distance. The  $P_d$  is suppressed due to the on-site Coulomb interaction, as expected. Its reduction is, however, not so considerably large compared to previous QMC studies [39] where the pairing correlation is almost annihilated for  $U = 4$ . We then turn to the case of less than half-filling. We show the results on  $8 \times 8$  with electron number  $N_e = 54$ . We show  $P_d$  as a function of the distance in Fig.49 ( $N_e = 54$ ). In the scale of this figure,  $P_d$  for  $U > 0$  is almost the same as that of the non-interacting case, and is enhanced slightly for large

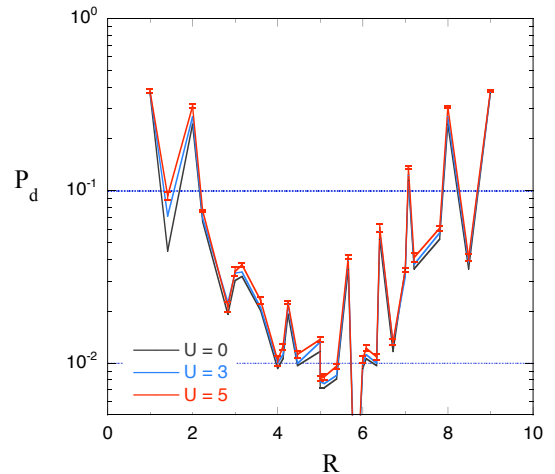


FIG. 50: Pair correlation function  $P_d$  as a function of the distance  $R = |\ell|$  on  $10 \times 10$  lattice for  $N_e = 82$  and  $t' = -0.2$ . The strength of the Coulomb interaction is  $U = 0, 3$  and  $5$ .

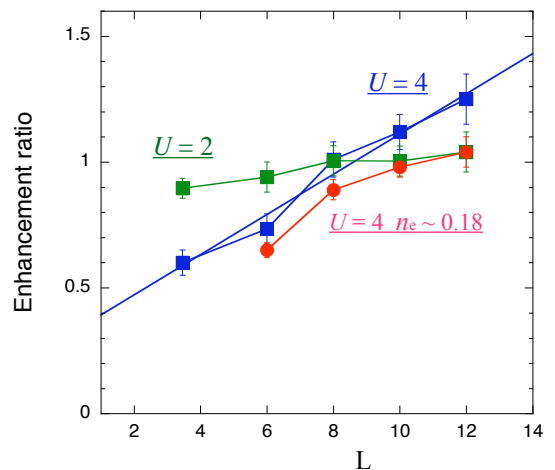


FIG. 51: Enhancement ratio of pair correlation function  $P_d|U/P_d|U=0$  as a function of the linear system size  $L$  for  $U = 4$  and  $U = 2$ . The electron density  $n_e$  is about  $0.8$ :  $n_e \sim 0.8$  for squares. The data for  $U = 4$  and  $n_e \sim 0.18$  are also shown by circles.

$U$ . Our results indicate that the pairing correlation is not suppressed and is indeed enhanced by the Coulomb interaction  $U$ , and its enhancement is very small.

The Fig.50 shows  $P_d$  on  $10 \times 10$  lattice. This also indicates that the pairing correlation function is enhanced for  $U > 0$ . There is a tendency that  $P_d$  is easily suppressed as the system size becomes small. We estimated the enhancement ratio compared to the non-interacting case  $P_d(\ell)|U/P_d(\ell)|U=0$  at  $|\ell| \sim L/2$  for  $n_e \sim 0.8$  as shown in Fig.51. This ratio increases as the system size is increased. To compute the enhancement, we picked the sites, for example on  $8 \times 8$  lattice,  $\ell = (3, 2), (4, 0), (4, 1), (3, 3), (4, 2), (4, 3), (5, 0), (5, 1)$  with  $|\ell| \sim 4 - 5$  and evaluate the mean value. In our computations, the ratio in-

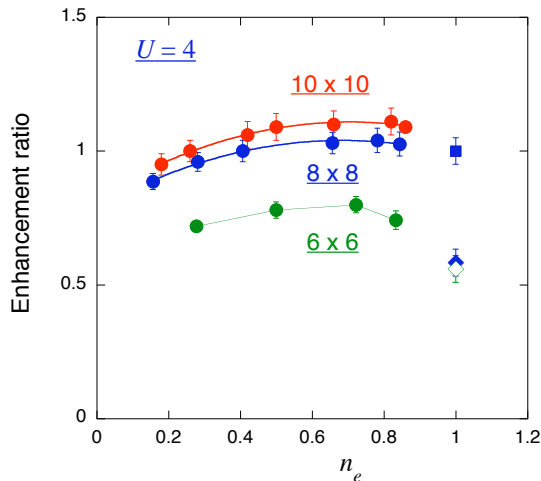


FIG. 52: Enhancement ratio of pair correlation function  $P_d|_U/P_d|_{U=0}$  as a function of the electron density  $n_e$ . We adopt  $t' = -0.2$  and  $U = 4$ . For the half-filled case, the diamonds show that for  $t' = 0$  on  $8 \times 8$  lattice (solid diamond) and  $6 \times 6$  lattice (open diamond). The square is for  $t' = -0.2$  on  $8 \times 8$  and  $10 \times 10$  where there is no enhancement.

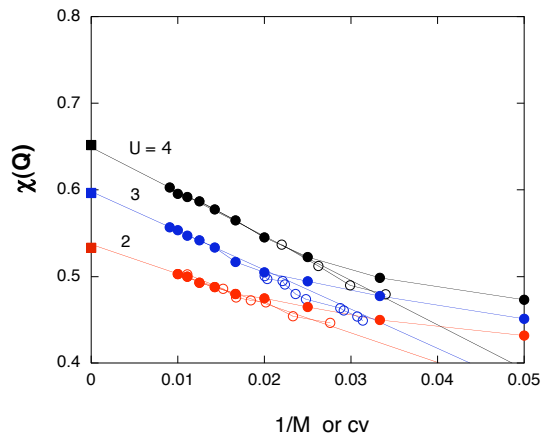


FIG. 53: Spin susceptibility  $\chi(Q)$  as a function of  $1/M$  or the variance  $v$  for a  $6 \times 2$  lattice with the periodic boundary condition. The number of electrons is 10. We set  $\Delta\tau = 0.01$ . The solid circles and open circles are obtained by using the QMC method and the QMD method, respectively. The squares indicate exact values. The variance  $v$  is multiplied by a numerical constant. We set  $U = 2, 3,$  and  $4$  in units of  $t$ .

creases almost linearly indicating a possibility of superconductivity. This indicates  $P_d(\ell) \sim LP_d(\ell) \sim \ell P_d(\ell)$  for  $\ell \sim L$ . Because  $P_d(\ell)|_{U=0} \sim 1/|\ell|^3$ , we obtain  $P_d(\ell) \sim \ell P_d(\ell) \sim 1/|\ell|^2$  for  $|\ell| \sim L$ . This indicates that the exponent of the power law is 2. When  $U = 2$ , the enhancement is small and is almost independent of  $L$ . In the low density case, the enhancement is also suppressed being equal to 1. In Fig.52, the enhancement ratio is shown as a function of the electron density  $n_e$  for  $U = 4$ . A dome structure emerges even in small systems. The square in Fig.52 indicates the result for the half-filled

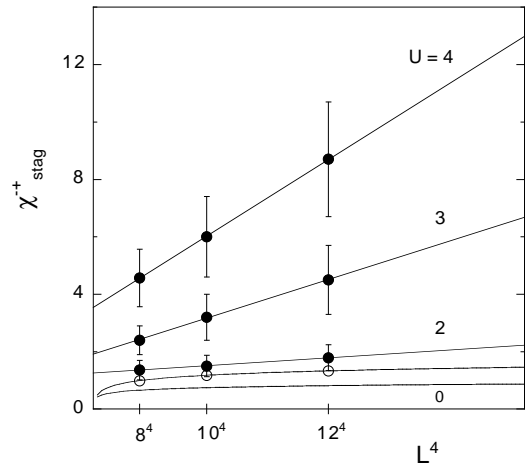


FIG. 54: Staggered spin susceptibility  $\chi_{stag}^{-+}$  as a function of  $L^4$  at half-filling with  $t' = 0$  for  $U = 2, 3,$  and  $4$ . We use the periodic and antiperiodic boundary conditions in the  $x$  and  $y$  directions, respectively. The lowest line is for  $U = 0$ , which is fitted by a logarithmic curve. The open circles show the results for the Gutzwiller function with  $U = 4$ , which exhibits a logarithmic dependence.

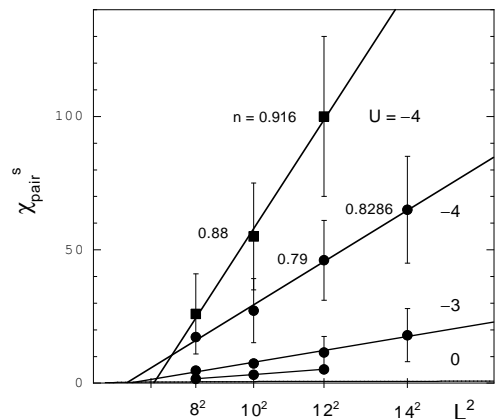


FIG. 55: Isotropic  $s$ -wave susceptibility  $\chi_{pair}^s$  as a function of  $L^2$  for the negative- $U$  Hubbard model with  $U = -2, -3,$  and  $-4$ , and  $t' = 0$ . The circles indicate the results for  $n_e \sim 0.8$ , where we use the periodic boundary condition in both the  $x$  and  $y$  directions, and the chemical potential is set at the center of the level spacing between adjacent energy levels. The lowest dotted line is for  $U = 0$  ( $n_e \sim 0.75$ ), which is fitted by a logarithmic curve, that is,  $\chi_{pair}^s \sim \log(L)$ . We show  $\chi_{pair}^s$  for  $n_e \sim 0.9$  and  $U = -4$  by squares, where the boundary condition is antiperiodic in one direction and periodic in the other direction.

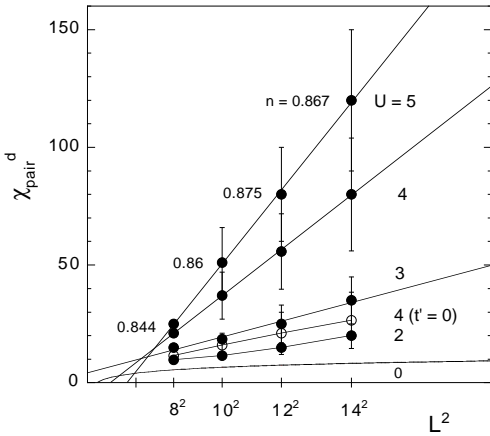


FIG. 56: The  $d$ -wave susceptibility  $\chi_{pair}^d$  as a function of  $L^2$  for the repulsive- $U$  Hubbard model with  $U = 2, 3, 4$ , and  $5$ . We use the periodic boundary condition in both the  $x$  and  $y$  directions. The solid circles present the results with  $t' = -0.2$  and  $n_e \sim 0.87$  for  $U = 2, 3, 4$  and  $5$ . For the solid squares the parameters are  $t' = -0.1$  and  $n_e \sim 0.82$  with  $U = 4$ . The open squares are for  $t' = -0.2$ ,  $n_e \sim 1$  (near half-filling) and  $U = 4$ . The open circles indicate the results for  $t' = 0$ ,  $n_e \sim 0.85$  and  $U = 4$ . The lowest line for  $U = 0$  is fitted by a logarithmic curve:  $\chi_{pair}^d \sim \log(L)$ .

case with  $t' = -0.2$  on  $8 \times 8$  lattice. This is the open shell case and causes a difficulty in computations as a result of the degeneracy due to partially occupied electrons. The inclusion of  $t' < 0$  enhances  $P_d$  compared to the case with  $t' = 0$  on  $8 \times 8$  lattice.  $P_d$  is, however, not enhanced over the non-interacting case at half-filling. This also holds for  $10 \times 10$  lattice where the enhancement ratio  $\sim 1$ . This indicates the absence of superconductivity at half-filling.

#### D. Spin Susceptibility

We propose a method to compute the magnetic susceptibility at absolute zero ( $T = 0$ ). [178] We add the source term  $H_1$  to the Hamiltonian as follows

$$H_1 = g \sum_j c_{j\uparrow}^\dagger c_{j\downarrow} e^{iq \cdot R_j} + \text{h.c.} = g(S_{-\mathbf{q}}^+ + \text{h.c.}), \quad (101)$$

where  $g$  is a small real number of the order  $10^{-3}$  or  $10^{-4}$ . We calculate  $-\langle S_{\mathbf{q}}^- \rangle / g$  in the ground state, which is, as shown by the linear response theory, the magnetic susceptibility

$$-\langle S_{\mathbf{q}}^- \rangle / g = \int_{-\infty}^{\infty} dt G_{ret}(t, \mathbf{q}) \Big|_{T \rightarrow 0} = \chi^{-+}(\mathbf{q}, \omega = 0) \Big|_{T \rightarrow 0}, \quad (102)$$

in the limit of small  $g$ , where  $G_{ret}$  is the retarded Green function and  $\chi^{-+}(\mathbf{q}, \omega)$  is the dynamical susceptibility,

$$\chi^{-+}(\mathbf{q}, \omega) = i \int_0^{\infty} dt e^{i\omega t} \langle [S_{\mathbf{q}}^-(t), S_{-\mathbf{q}}^+(0)] \rangle. \quad (103)$$

Indeed, the above formula gives the correct spin susceptibility  $\chi^{-+}(\mathbf{q}, \omega = 0)$  on the finite lattice for the noninteracting case, which is given by  $\sum_k (f(\xi_{k+q}) - f(\xi_k)) / (\xi_k - \xi_{k+q})$  with the Fermi distribution function  $f(\xi)$ . We calculate  $-\langle S_{\mathbf{q}}^- \rangle / g$  by using the quantum Monte Carlo method to obtain  $\chi^{-+}(\mathbf{q}, \omega = 0)$ .

We examine the results obtained for the susceptibilities. Figure 53 shows the spin susceptibility  $\chi(Q) = \chi^{-+}(Q, \omega = 0)$  for  $Q = (\pi, \pi)$  on a  $6 \times 2$  lattice as a function of  $1/m$  or the energy variance  $v$ . The number of electrons is 10. The expectation values agree well with exact values given by the exact diagonalization method.

We now compute the staggered susceptibility  $\chi_{stag}^{-+}$  by adding the source term  $H_1 = g \sum_j (c_{j\uparrow}^\dagger c_{j\downarrow} (-1)^{j_x + j_y} + \text{h.c.})$  to the Hamiltonian, where  $j = (j_x, j_y)$ . Here we set the periodic and antiperiodic boundary conditions in the  $x$  and  $y$  directions, respectively, to avoid a numerical difficulty caused by the degeneracy between states  $\mathbf{k}$  and  $\mathbf{k} + Q$  where  $Q = (\pi, \pi)$ . It has been shown that a long-range spin correlation exists in the ground state of the half-filled Hubbard model with  $t' = 0$  for  $U > 0$  [40, 41, 179, 180]. In the case  $U = 0$ ,  $\chi_{stag}^{-+}$  exhibits a double logarithmic behavior  $(\log(L))^2$ .  $\chi_{stag}^{-+}$  is shown as a function of  $L$  in Fig.54 for  $U = 2, 3$ , and  $4$ . The obtained values are well fitted by  $L^4$  and  $\chi_{stag}^{-+}$  diverges in the limit of a large system size  $L$ :

$$\chi_{stag}^{-+} \sim L^4. \quad (104)$$

This result is consistent with the existence of the long-range spin correlation for  $U > 0$  [179, 180]. The degree of divergence of  $\chi_{stag}^{-+}$  is beyond the criterion of the Kosterlitz-Thouless transition, and thus the long-range order represented by  $\chi_{stag}^{-+}$  belongs to a different category. The  $L^4$  behavior of  $\chi_{stag}$  is consistent with the predictions of perturbation theory in the 2D non-linear sigma model at low temperatures [181].

#### E. Pair Susceptibility

In this section we consider a method to evaluate the pair susceptibility  $\chi_{pair}$  at  $T = 0$ . In order to compute the pair susceptibility, we use an electron-hole transformation for the down spin,  $c_{i\downarrow} = d_i^\dagger$ , whereas the up-spin electrons are unaltered,  $c_{i\uparrow} = c_i$ . For the on-site  $s$ -wave pairing, the source term is given by the following expression

$$H_1^s = g \sum_i (c_i^\dagger d_i + \text{h.c.}). \quad (105)$$

For the anisotropic  $d$ -wave pairing, we add

$$\begin{aligned} H_1^d &= g \sum_{i, \mu (= \pm x, \pm y)} (a_\mu c_{i+\mu}^\dagger c_{i\downarrow}^\dagger + \text{h.c.}) \\ &= g \sum_{i, \mu (= \pm x, \pm y)} (a_\mu c_{i+\mu}^\dagger d_i + \text{h.c.}), \end{aligned} \quad (106)$$

where  $a_{\pm x} = 1$  and  $a_{\pm y} = -1$ . The  $s$ -wave and  $d$ -wave pair susceptibility are respectively:

$$\begin{aligned}\chi_{pair}^s &= -\frac{1}{g} \frac{1}{N} \sum_i (\langle c_i^\dagger d_i \rangle + \text{h.c.}), \\ \chi_{pair}^d &= -\frac{1}{g} \frac{1}{N} \sum_{i,\mu(=\pm x,\pm y)} (a_\mu \langle c_{i+\mu}^\dagger d_i \rangle + \text{h.c.}).\end{aligned}\quad (107)$$

Using the Fourier transformation, the source term for the pair potential is written as follows  $H_1^a = g \sum_k z_k (c_{-k\downarrow}^\dagger c_{k\uparrow}^\dagger + \text{h.c.})$  for  $a = s$  or  $d$  with the  $k$ -dependence factor  $z_k$ . If we define  $\Delta_k = \langle c_{k\uparrow} c_{-k\downarrow} \rangle$ , then for a small value of  $g$ , we have the following

$$\Delta_k/g = -\sum_{k'} z_{k'} \int_{-\infty}^{\infty} dt' G_{ret}(t-t'; k, k'), \quad (108)$$

where

$$G_{ret}(t-t'; k, k') = i\theta(t-t') \langle [b_k(t), b_{k'}^\dagger(t')] \rangle, \quad (109)$$

for  $b_k = c_{k\uparrow} c_{-k\downarrow}$  and  $b_k(t) = e^{iHt} b_k e^{-iHt}$ . On the basis of analytic continuation, using the thermal Green function,  $\Delta_k$  is written as

$$\Delta_k/g = -\sum_{k'} \int_0^\beta d\tau e^{i\omega_n \tau} \langle T_\tau b_k(\tau) b_{k'}^\dagger(0) \rangle_{i\omega_n \rightarrow 0}. \quad (110)$$

In the noninteracting system, this formula exhibits logarithmic divergence on the finite lattice  $L \times L$ :  $\chi_{pair} = A \langle |z_k|^2 \rangle \log(cL)$  with constants  $A$  and  $c$ , which can be confirmed by numerical estimations on finite systems.

In the Kosterlitz-Thouless theory, the susceptibility is scaled as follows[182, 183]:  $\chi \sim \xi^{2-\eta}$ , where  $\xi$  is the coherence length.  $\xi$  is of order  $L$  on a lattice  $L \times L$  if long-range coherence exists. The exponent  $\eta$  is expected to be 0 at absolute zero. Thus  $\chi$  scales as  $\chi \sim L^2$  in the ground state if the Kosterlitz-Thouless transition occurs at some temperature.

First, we investigate  $\chi_{pair}^s$  for the attractive Coulomb interaction  $U < 0$ . For this model, the existence of a Kosterlitz-Thouless transition has been predicted on the basis of quantum Monte Carlo methods[34, 183]. The results in Fig.55 show that the size dependence for  $t' = 0$  and  $n_e \sim 0.8$  is

$$\chi_{pair}^s \sim L^2, \quad (111)$$

which is consistent with previous studies, and shows the existence of a Kosterlitz-Thouless transition for the attractive interaction. At near half-filling,  $\chi_{pair}^s$  is more enhanced than that at  $n_e \sim 0.8$ . Second, let us investigate the  $d$ -wave pair susceptibility  $\chi_{pair}^d$  for the repulsive Coulomb interaction. Pair susceptibilities are sensitively dependent on the band structure, particularly the energy of the van Hove singularity, as a characteristic of two-dimensional systems. We compute  $\chi_{pair}^d$  at an electron density  $n_e \sim 0.87$ , a value near that of optimally doped

high-temperature cuprates. We set  $t' = -0.2$ . Figure 56 shows  $\chi_{pair}^d$  as a function of  $L^2$  for  $U = 2, 3, 4$ , and 5 with  $t' = -0.2$  and  $n_e \sim 0.87$ . This shows that

$$\chi_{pair}^d \sim L^2, \quad (112)$$

if  $U$  is moderately large. This result shows that a  $d$ -wave superconducting Kosterlitz-Thouless transition may exist for the repulsive interaction if we adjust the band parameters in the region of optimal doping.

## V. SUMMARY

We have investigated the superconductivity of electronic origin on the basis of the (single-band and three-band) two-dimensional Hubbard model. First, we employ the variational Monte Carlo method to clarify the phase diagram of the ground state of the Hubbard model. The superconducting condensation energy per site obtained by the Gutzwiller ansatz is reasonably close to experimental value  $0.17 \sim 0.26$  meV/site. We have examined the stability of striped and checkerboard states in the underdoped region. The relation of the incommensurability and hole density,  $\delta \sim x$ , is satisfied in the lower doped region. We have found that the  $4 \times 4$  period checkerboard spin modulation is stabilized in the two-dimensional Hubbard model with the Bi-2212 type band structure.

We have further performed investigation by using the quantum Monte Carlo method that is an exact unbiased method. We have presented an algorithm of the quantum Monte Carlo diagonalization to avoid the negative sign problem in quantum simulations of many-fermion systems. We have computed  $d$ -wave pair correlation functions. In the half-filled case  $P_d$  is suppressed for the repulsive  $U > 0$ , and when doped away from half-filling  $N_e < N$ ,  $P_d$  is enhanced slightly for  $U > 0$ . It is noteworthy that the correlation function  $P_d$  is indeed enhanced and is increased as the system size increases in the 2D Hubbard model. The enhancement ratio increases almost linearly  $\propto L$  as the system size is increased, which is an indication of the existence of superconductivity. Our criterion is that when the enhancement ratio as a function of the system size  $L$  is proportional to a certain power of  $L$ , superconductivity will be developed. This ratio depends on  $U$  and is reduced as  $U$  is decreased. The dependence on the band filling shows a dome structure as a function of the electron density. In the  $10 \times 10$  system, the ratio is greater than 1 in the range  $0.3 < n_e < 0.9$ . Let us also mention on superconductivity at half-filling. Our result indicates the absence of superconductivity in the half-filling case because there is no enhancement of pair correlation functions.

## Acknowledgment

We thank I. Hase, S. Koikegami, S. Koike and J. Kondo for stimulating discussions. This work was supported by a Grant-in Aid for Scientific Research from the Ministry

of Education, Culture, Sports, Science and Technology of Japan, and CREST Program of Japan Science and Technology Agency. A part of numerical calculations was

performed at the facilities in the Supercomputer Center of the Institute for Solid State Physics of the University of Tokyo.

- 
- [1] J. G. Bednorz and K. A. Müller, *Z. Phys.* **B64**, 189 (1986).
- [2] E. Dagotto, *Rev. Mod. Phys.* **66**, 763 (1994).
- [3] P. W. Anderson, *The Theory of Superconductivity in the High- $T_c$  Cuprates* (Princeton University Press, Princeton, 1997).
- [4] T. Moriya and K. Ueda, *Adv. Phys.* **49**, 555 (2000).
- [5] *The Physics of Superconductor* Vol.II, edited by K. H. Bennemann and J. B. Ketterson (Springer, Berlin, 2003).
- [6] G. R. Stewart, *Rev. Mod. Phys.* **56**, 755 (1984).
- [7] P. A. Lee, T. M. Rice, J. W. Serene, L. J. Sham and J. W. Wilkins, *Comments Cond. Matter Phys.* **12**, 99 (1986).
- [8] H. R. Ott, *Prog. Low Temp. Phys.* **11**, 215 (1987).
- [9] M. B. Maple, *Handbook on the Physics and Chemistry of Rare Earths* Vol. 30 (North-Holland, Elsevier, Amsterdam, 2000).
- [10] T. Ishiguro, K. Yamaji and G. Saito, *Organic Superconductors* (Springer-Verlag, Berlin, 1998).
- [11] C. C. Tsuei et al., *Phys. Rev. Lett.* **73**, 593 (1994).
- [12] D. A. Wollman et al., *Phys. Rev. Lett.* **74**, 797 (1995).
- [13] C. C. Tsuei and J. R. Kirtlry, *Phys. Rev. Lett.* **85**, 182 (2000).
- [14] T. Sato, T. Kamiyama, T. Takahashi, K. Kurahashi, and K. Yamada, *Science* **291**, 1517 (2001).
- [15] T. Yanagisawa, S. Koikegami, H. Shibata, S. Kimura, S. Kashiwaya, A. Sawa, N. Matsubara and K. Takita, *J. Phys. Soc. Jpn.* **70**, 2833 (2001).
- [16] G. Shirane, Y. Endoh, R. Birgeneau, M. A. Kastner, Y. Hidaka, M. Oka, M. Suzuki, and T. Murakami, *Phys. Rev. Lett.* **59**, 1613 (1987).
- [17] K. B. Lyons, P. A. Fleury, L. F. Schnccemeyer, and J. V. Waszczak, *Phys. Rev. Lett.* **60**, 732 (1988).
- [18] E. Manousakis and R. Salvadoe, *Phys. Rev. Lett.* **62**, 1310 (1989).
- [19] P. Prelovsek, *Phys. Lett.* **A126**, 287 (1988).
- [20] M. Inui and S. Doniach, *Phys. Rev.* **B38**, 6631 (1988).
- [21] T. Yanagisawa, *Phys. Rev. Lett.* **68**, 1026 (1992).
- [22] T. Yanagisawa and Y. Shimoi, *Phys. Rev.* **B48**, 6104 (1993).
- [23] T. Yanagisawa and Y. Shimoi, *Int. J. Mod. Phys.* **B10**, 3383 (1996) (<http://staff.aist.go.jp/t-yanagisawa/paper/sprevc.pdf>).
- [24] T. Yanagisawa, S. Koike, and K. Yamaji, *Phys. Rev.* **B64**, 184509 (2001).
- [25] J. M. Tranquada, B. J. Sternlieb, J. D. Axe, Y. Nakamura, and S. Uchida, *Nature* **375**, 561 (1995).
- [26] J. Hubbard, *Proc. Roy. Soc.* **A276**, 238 (1963); **A277**, 237 (1964); **A281**, 401(1964).
- [27] J. E. Hirsch, *Phys. Rev. Lett.* **51**, 1900 (1983).
- [28] J. E. Hirsch: *Phys. Rev.* **B31**, 4403 (1985).
- [29] S. Sorella, E. Tosatti, S. Baroni, R. Car and M. Parrinell, *Int. J. Mod. Phys.* **B2**, 993 (1988).
- [30] S. R. White, D. J. Scalapino, R. L. Sugar, E. Y. Loh, J. E. Gubernatis, and R. T. Scalettar, *Phys. Rev.* **B40**, 506 (1989).
- [31] M. Imada and Y. Hatsugai, *J. Phys. Soc. Jpn.* **58**, 3752 (1989).
- [32] S. Sorella, S. Baroni, R. Car and M. Parrinello, *Europhys. Lett.* **8**, 663 (1989).
- [33] E. Y. Loh, J. E. Gubernatis, R. T. Scalettar, S. R. White, D. J. Scalapino, and R. L. Sugar, *Phys. Rev.* **B41**, 9301 (1990).
- [34] A. Moreo, D. J. Scalapino, and E. Dagotto, *Phys. Rev.* **B56**, 11442 (1991).
- [35] N. Furukawa and M. Imada, *J. Phys. Soc. Jpn.* **61**, 3331 (1992).
- [36] A. Moreo, *Phys. Rev.* **B45**, 5059 (1992).
- [37] S. Fahy and D. R. Hamann, *Phys. Rev.* **B43**, 765 (1991).
- [38] S. Zhang, J. Carlson and J. E. Gubernatis, *Phys. Rev.* **B55**, 7464 (1997).
- [39] S. Zhang, J. Carlson and J. E. Gubernatis, *Phys. Rev. Lett.* **78**, 4486 (1997).
- [40] T. Kashima and M. Imada, *J. Phys. Soc. Jpn.* **70**, 2287 (2001).
- [41] T. Yanagisawa, *Phys. Rev.* **B75**, 224503 (2007) (arXiv:0707.1929).
- [42] T. Yanagisawa, *New J. Phys.* **15**, 033012 (2013).
- [43] H. Yokoyama and H. Shiba, *J. Phys. Soc. Jpn.* **56**, 1490 (1987); *ibid.* **56**, 3582 (1987).
- [44] C. Gros, R. Joynt, and T. M. Rice, *Phys. Rev.* **B36**, 381 (1987).
- [45] T. Nakanishi, K. Yamaji and T. Yanagisawa, *J. Phys. Soc. Jpn.* **66**, 294 (1997).
- [46] K. Yamaji, T. Yanagisawa, T. Nakanishi and S. Koike, *Physica* **C304**, 225 (1998).
- [47] T. Yanagisawa, S. Koike and K. Yamaji, *J. Phys.: Condens. Matter* **14**, 21 (2002).
- [48] T. Yanagisawa, S. Koike, S. Koikegami and K. Yamaji, *Phys. Rev.* **B67**, 132400 (2003).
- [49] T. Yanagisawa, M. Miyazaki and K. Yamaji, *J. Phys. Soc. Jpn.* **74**, 835 (2005).
- [50] M. Miyazaki, K. Yamaji and T. Yanagisawa, *J. Phys. Soc. Jpn.* **73**, 1643 (2004).
- [51] K. Yamaji and Y. Shimoi, *Physica* **C222**, 349 (1994).
- [52] K. Yamaji, Y. Shimoi and T. Yanagisawa, *Physica* **C235-240**, 2221 (1994).
- [53] S. Koike, K. Yamaji and T. Yanagisawa, *J. Phys. Soc. Jpn.* **68**, 1657 (1999).
- [54] S. Koike, K. Yamaji and T. Yanagisawa, *J. Phys. Soc. Jpn.* **69**, 2199 (2000).
- [55] R. M. Noack, S. R. White, and D. J. Scalapino, *Physica* **C270**, 281 (1996).
- [56] R. M. Noack, N. Bulut, D. J. Scalapino, and M. G. Zacher, *Phys. Rev.* **B56**, 7162 (1997).
- [57] K. Kuroki, T. Kimura and H. Aoki, *Phys. Rev.* **B54**, 15641 (1996),
- [58] S. Daul and D. J. Scalapino, *Phys. Rev.* **B62**, 8658 (2000).
- [59] K. Sano, Y. Ono, and Y. Yamada, *J. Phys. Soc. Jpn.* **74**, 2885 (2005).

- [60] N. Bulut, Adv. in Phys. **51**, 1587 (2002).
- [61] T. Aimi and M. Imada, J. Phys. Soc. Jpn. **76**, 113708 (2007).
- [62] J. Kondo, J. Phys. Soc. Jpn. **70**, 808 (2001).
- [63] R. Hlubina, Phys. Rev. B **59**, 9600 (1999).
- [64] S. Koikegami and T. Yanagisawa, J. Phys. Soc. Jpn. **70**, 3499 (2001); **71**, 761 (2002) (E).
- [65] S. Koikegami and T. Yanagisawa, J. Phys. Soc. Jpn. **75**, 034715 (2006).
- [66] T. Yanagisawa, New J. Phys. **10**, 023014 (2008).
- [67] A. B. Harris and R. V. Lange, Phys. Rev. **157**, 295 (1967).
- [68] M. C. Gutzwiller, Phys. Rev. Lett. **10**, 159 (1963).
- [69] J. Kanamori, Prog. Theor. Phys. **30**, 275 (1963).
- [70] H. Bethe, Z. Phys. **71**, 205 (1931).
- [71] C. N. Yang, Phys. Rev. Lett. **19**, 1312 (1967).
- [72] E. H. Lieb and F. Y. Wu, Phys. Rev. Lett. **20**, 1445 (1968).
- [73] H. J. Schulz, Phys. Rev. Lett. **64**, 2831 (1990).
- [74] H. Frahm and V. E. Korepin, Phys. Rev. B **42**, 10552 (1990).
- [75] N. Kawakami and S. K. Yang, Phys. Lett. A **148**, 359 (1990).
- [76] F. D. M. Haldane, J. Phys. C **14**, 2585 (1981).
- [77] V.J. Emery: Phys. Rev. Lett. **58**, 2794 (1987).
- [78] L.H. Tjeng, H. Eskes, and G.A. Sawatzky, *Strong Correlation and Superconductivity* edited by H. Fukuyama, S. Maekawa and A.P. Malozemoff (Springer, Berlin Heidelberg, 1989), p.33.
- [79] W.H. Stephan, W. Linden and P. Horsch, Phys. Rev. B **39**, 2924 (1989).
- [80] J.E. Hirsch, E.Y. Loh, D.J. Scalapino and S. Tang, Phys. Rev. B **39**, 243 (1989).
- [81] R.T. Scalettar, D.J. Scalapino, R.L. Sugar and S.R. White, Phys. Rev. B **44**, 770 (1991).
- [82] G. Dopf, A. Muramatsu and W. Hanke, Phys. Rev. B **41**, 9264 (1990).
- [83] G. Dopf, A. Muramatsu and W. Hanke, Phys. Rev. Lett. **68**, 353 (1992).
- [84] T. Asahata, A. Oguri and S. Maekawa, J. Phys. Soc. Jpn. **65**, 365 (1996).
- [85] K. Kuroki and H. Aoki, Phys. Rev. Lett. **76**, 4400 (1996).
- [86] T. Takimoto and T. Moriya, J. Phys. Soc. Jpn. **66**, 2459 (1997).
- [87] M. Guerrero, J.E. Gubernatis and S. Zhang, Phys. Rev. B **57**, 11980 (1998).
- [88] S. Koikegami and K. Yamada, J. Phys. Soc. Jpn. **69**, 768 (2000).
- [89] M.S. Hybertsen, E.B. Stechel, M. Schlüter and D.R. Jennison, Phys. Rev. B **41**, 11068 (1990).
- [90] H. Eskes, G.A. Sawatzky and L.F. Feiner, Physica C **160**, 424 (1989).
- [91] A.K. McMahan, J.F. Annett and R.M. Martin, Phys. Rev. B **42**, 6268 (1990).
- [92] D. Ceperley, G.V. Chester and K.H. Kalos, Phys. Rev. B **16**, 3081 (1977).
- [93] C.J. Umrigar, K.G. Wilson and J.W. Wilkins, Phys. Rev. Lett. **60**, 1719 (1988).
- [94] R. Blankenbecler, D.J. Scalapino and R.L. Sugar, Phys. Rev. D **24**, 2278 (1981).
- [95] T. Yanagisawa, S. Koike and K. Yamaji, J. Phys. Soc. Jpn. **67**, 3867 (1998).
- [96] T. Yanagisawa, S. Koike and K. Yamaji, J. Phys. Soc. Jpn. **68**, 3608 (1999).
- [97] K. Yamaji, T. Yanagisawa and S. Koike, Physica B **284-288**, 415 (2000).
- [98] L.F. Feiner, J.H. Jefferson and R. Raimondi, Phys. Rev. B **53**, 8751 (1996).
- [99] J.W. Loram, K.A. Mirza, J.R. Cooper and W.Y. Liang, Phys. Rev. Lett. **71**, 1470 (1993).
- [100] P.W. Anderson, Science **279**, 1196 (1998).
- [101] Z. Hao, J.R. Clem, M.W. McElfresh, L. Civale, A.P. Malozemoff and F. Holtzberg, Phys. Rev. B **43**, 2844 (1991).
- [102] H. Yokoyama and M. Ogata, J. Phys. Soc. Jpn. **65**, 3615 (1996).
- [103] T. Matsuzaki, N. Momono, M. Oda and M. Ido, J. Phys. Soc. Jpn. **73**, 2232 (2004).
- [104] T. Tohyama and S. Maekawa, Supercond. Sci. Technol. **13**, 17 (2000).
- [105] M. Miyazaki, K. Yamaji and T. Yanagisawa, J. Phys. Chem. Solids **63**, 1403 (2002).
- [106] T. Yanagisawa, M. Miyazaki and K. Yamaji, J. Phys. Soc. Jpn. **78**, 013706 (2009).
- [107] D. J. Singh and W. E. Pickett, Physica C **203**, 193 (1992).
- [108] N. E. Hussey et al., Nature **425**, 814 (2003).
- [109] M. Plate et al., Phys. Rev. Lett. **95**, 07001 (2005).
- [110] W. S. Lee et al., arXiv: cond-mat/0600347 (2006).
- [111] K. Yamaji, T. Yanagisawa, M. Miyazaki and R. Kadono, Physica C **468**, 1125 (2008).
- [112] K. Yamaji, T. Yanagisawa, M. Miyazaki and R. Kadono, J. Phys. Soc. Jpn. **80**, 083702 (2011).
- [113] M. Fabrizio, A. Parola and T. Tosatti, Phys. Rev. B **46**, 3159 (1992).
- [114] M. Fabrizio, Phys. Rev. B **48**, 15838 (1993).
- [115] T. Yanagisawa, Y. Shimoi and K. Yamaji, Phys. Rev. B **52**, 3860 (1995).
- [116] L. Balents and M.P.A. Fisher, Phys. Rev. B **53**, 12133 (1996).
- [117] G.-q. Zheng, Y. Kitaoka, K. Ishida and K. Asayama, J. Phys. Soc. Jpn. **64**, 2524 (1995).
- [118] J. Tranquada, J.D. Axe, N. Ichikawa, Y. Nakamura, S. Uchida and B. Nachumi, Phys. Rev. B **54**, 7489 (1996).
- [119] T. Suzuki, T. Goto, K. Chiba, T. Fukase, H. Kimura, K. Yamada, M. Ohashi and Y. Yamaguchi, Phys. Rev. B **57**, 3229 (1998).
- [120] K. Yamada, C.H. Lee, K. Kurahashi, J. Wada, S. Wakimoto, S. Ueki, H. Kimura and Y. Endoh, Phys. Rev. B **57**, 6165 (1998).
- [121] M. Arai, T. Nishijima, Y. Endoh, T. Egami, S. Tajima, K. Tomimoto, Y. Shiohara, M. Takahashi, A. Garrett and S.M. Bennington, Phys. Rev. Lett. **83**, 608 (1999).
- [122] H.A. Mook, D. Pengcheng, F. Dogan and R.D. Hunt, Nature **404**, 729 (2000).
- [123] S. Wakimoto, R.J. Birgeneau, M.A. Kastner, Y.S. Lee, R. Erwin, P.M. Gehring, S.H. Lee, M. Fujita, K. Yamada, Y. Endoh, K. Hirota and G. Shirane, Phys. Rev. B **61**, 3699 (2000).
- [124] T. Noda, H. Eisaki and S. Uchida, Science **286**, 265 (1999).
- [125] X.J. Zhou, P. Bogdanov, S.A. Keller, T. Noda, H. Eisaki, S. Uchida, Z. Hussain and Z.X. Shen, Science **286**, 268 (1999).
- [126] C. Niedermayer, C. Bernhard, T. Blasius, A. Golnik, A. Moodenbauch and J.I. Budnick, Phys. Rev. Lett. **80**, 3843 (1998).

- [127] H. Kimura *et al.*, Phys. Rev. B**59**, 6517 (1999).
- [128] H. Matsushita, H. Kimura, M. Fujita, K. Yamada, K. Hirota and Y. Endoh, J. Phys. Chem. Solids **60**, 1079 (1999).
- [129] M. Matsuda, M. Fujita, K. Yamada, R.J. Birgeneau, M.A. Kastner, H. Hirai, Y. Endoh, S. Wakimoto and G. Shirane, Phys. Rev. B**62**, 9148 (2000).
- [130] M. Fujita, K. Yamada, H. Hiraka, P. M. Gehring, S. H. Leem S. Wakimoto and G. Shigane, Phys. Rev. B**65**, 064505 (2002).
- [131] T. Giamarchi and C. Lhuillier, Phys. Rev. B**43**, 12943 (1991).
- [132] K. Machida, Physica C**158**, 192 (1989).
- [133] D. Poilblanc and T.M. Rice, Phys. Rev. B**39**, 9749 (1989).
- [134] M. Kato, K. Machida, H. Nakanishi and M. Fujita, J. Phys. Soc. Jpn. **59**, 1047 (1990).
- [135] H. Schulz, Phys. Rev. Lett. **64**, 1445 (1990).
- [136] J. Zaanen and A.M. Oles, Annalen der Physik **508**, 224 (1996).
- [137] M. Ichioka and K. Machida, J. Phys. Soc. Jpn. **68**, 4020 (1999).
- [138] S. White and D.J. Scalapino, Phys. Rev. Lett. **80**, 1272 (1998).
- [139] S. White and D.J. Scalapino, Phys. Rev. Lett. **81**, 3227 (1998).
- [140] C. S. Hellberg and E. Manousakis, Phys. Rev. Lett. **83**, 132 (1999).
- [141] K. Kobayashi and H. Yokoyama, Physica B**259-261**, 506 (1999).
- [142] A. Himeda, T. Kato and M. Ogata, Phys. Rev. Lett. **88**, 117001 (2002).
- [143] W. Loram, K.A. Mirza, J.R. Cooper, N. Athanasopoulou and W. Liang, *Proc. 10th Ann. HTS Workshop* (World Scientific, Singapore, 1996) p.341.
- [144] M. Miyazaki, K. Yamaji, T. Yanagisawa and K. Yonemitsu, Physcs Procedia **27**, 64 (2012).
- [145] H. Mukuda *et al.*, Phys. Rev. Lett. **96**, 087001 (2006).
- [146] J. E. Hoffman *et al.*, Science **295**, 466 (2002).
- [147] W. D. Wise *et al.*, Nature Phys. **4**, 696 (2008).
- [148] T. Hanaguri *et al.*, Nature **430**, 1001 (2004).
- [149] S. R. White and D. J. Scalapino, Phys. Rev. B**70**, 220506 (2004).
- [150] G. Seibold, J. Lorenzana and M. Grilli, Phys. Rev. B**75**, 100505 (2007).
- [151] M. Miyazaki, K. Yamaji, T. Yanagisawa and R. Kadono, J. Phys. Soc. Jpn. **78**, 043706 (2009).
- [152] R. Jastrow, Phys. Rev. **55**, 1479 (1955).
- [153] H. Ohtsuka, J. Phys. Soc. Jpn. **61**, 1645 (1992).
- [154] H. De Raedt, Phys. Rep. **127**, 233 (1985).
- [155] H. Yokoyama and H. Shiba, J. Phys. Soc. Jpn. **57**, 2482 (1988).
- [156] J. B. Torrance and R. M. Metzger, Phys. Rev. Lett. **63**, 1515 (1989).
- [157] D.J. Scalapino, E. Loh and J.E. Hirsch, Phys. Rev. B**34**, 8190 (1986).
- [158] H. Shimahara and S. Takada, J. Phys. Soc. Jpn. **57**, 1044 (1988).
- [159] P. Monthoux, A.V. Balatsky and D. Pines, Phys. Rev. Lett. **67**, 3448 (1991).
- [160] N.E. Bickers, D.J. Scalapino and S.R. White, Phys. Rev. Lett. **62**, 961 (1989).
- [161] C.-H. Pao and N.E. Bickers, Phys. Rev. B**49**, 1586 (1994); Phys. Rev. Lett. **72**, 1870 (1994).
- [162] P. Monthoux and D.J. Scalapino, Phys. Rev. Lett. **72**, 1874 (1994).
- [163] Y. Yanase and K. Yamada, J. Phys. Soc. Jpn. **68**, 2999 (1999).
- [164] K. Miyake, S. Schmidt-Rink and C.M. Varma, Phys. Rev. B**34**, 6554 (1986).
- [165] T. Moriya, Y. Takahashi and K. Ueda, J. Phys. Soc. Jpn. **59**, 2905 (1990).
- [166] T. Hotta, J. Phys. Soc. Jpn. **62**, 4414 (1993).
- [167] T. Jujo, S. Koikegami and K. Yamada, J. Phys. Soc. Jpn. **68**, 1331 (1999).
- [168] T. Nomura and K. Yamada, J. Phys. Soc. Jpn. **69**, 3678 (2000).
- [169] S. Koikegami, Y. Yoshida and T. Yanagisawa, Phys. Rev. B**67**, 134517 (2003).
- [170] S. Koikegami and T. Yanagisawa, J. Phys. Soc. Jpn. **79**, 064701 (2010).
- [171] K. Yamaji and T. Yanagisawa, Physica C, (2013) in press (<http://dx.doi.org/10.1016/j.physc.2013.04.017>).
- [172] S. Koike *et al.*, Physica C**388-389**, 65 (2003).
- [173] E. Pavarini *et al.*, Phys. Rev. Lett. **87**, 047003 (2001).
- [174] T. Mizusaki, M. Honma and T. Otsuka, Phys. Rev. C**53**, 2786 (1986).
- [175] S. Sorella, Phys. Rev. B**64**, 024512 (2001).
- [176] D. E. Goldberg, *Genetic Algorithms in Search, Optimization and Machine Learning* (Addison-Wesley, Boston, 1989).
- [177] A. Parola, S. Sorella, S. Baroni, R. Car, M. Parrinello and E. Tosatti, Physica C**162-164**, 771 (1989).
- [178] T. Yanagisawa, J. Phys. Soc. Jpn. **79**, 063708 (2010).
- [179] J. A. Riera and A. P. Young, Phys. Rev. B**39**, 9697 (1989).
- [180] M. Calandra Buonauro and S. Sorella, Phys. Rev. B**57**, 11446 (1998).
- [181] P. Hasenfratz and F. Niedernayer, Z. Physik B**92** (1993) 91.
- [182] J. M. Kosterlitz and D. J. Thouless, J. Phys. C**6** (1973) 1181.
- [183] S. Chandrasekharan and J. C. Osborn, Phys. Rev. B**66** (2002) 045113.